

DISA: Accurate Learning-based Static Disassembly with Attentions

Peicheng Wang*
Xidian University
Xi'an, Shaanxi, China
732176028@qq.com

Monika Santra*
The Pennsylvania State University
University Park, PA, USA
monikas@psu.edu

Mingyu Liu
Xidian University
Xi'an, Shaanxi, China
23151214197@stu.xidian.edu.cn

Cong Sun†
Xidian University
Xi'an, Shaanxi, China
suncong@xidian.edu.cn

Dongrui Zeng
Palo Alto Networks, Inc.
Santa Clara, CA, USA
dzeng@paloaltonetworks.com

Gang Tan†
The Pennsylvania State University
University Park, PA, USA
gtan@psu.edu

Abstract

For reverse engineering related security domains, such as vulnerability detection, malware analysis, and binary hardening, disassembly is crucial yet challenging. The fundamental challenge of disassembly is to identify instruction and function boundaries. Classic approaches rely on file-format assumptions and architecture-specific heuristics to guess the boundaries, resulting in incomplete and incorrect disassembly, especially when the binary is obfuscated. Recent advancements of disassembly have demonstrated that deep learning can improve both the accuracy and efficiency of disassembly. In this paper, we propose DISA, a new learning-based disassembly approach that uses the information of superset instructions over the multi-head self-attention to learn the instructions' correlations, thus being able to infer function entry-points and instruction boundaries. DISA can further identify instructions relevant to memory block boundaries to facilitate an advanced block-memory model based value-set analysis for an accurate control flow graph (CFG) generation. Our experiments show that DISA outperforms prior deep-learning disassembly approaches in function entry-point identification, especially achieving 9.1% and 13.2% F1-score improvement on binaries respectively obfuscated by the disassembly desynchronization technique and popular source-level obfuscator. By achieving an 18.5% improvement in the memory block precision, DISA generates more accurate CFGs with a 4.4% reduction in Average Indirect Call Targets (AICT) compared with the state-of-the-art heuristic-based approach.

CCS Concepts

• Security and privacy → Software reverse engineering.

Keywords

Reverse Engineering; Disassembly; Points-to Analysis; Deep Learning; Static Analysis

1 Introduction

Disassembly is a fundamental step in analyzing, rewriting, and hardening binary programs. The static disassembly procedure comprises different sub-tasks [6, 43]. In these sub-tasks, identifying the function and instruction boundaries are the most fundamental tasks and prerequisites of control flow graph (CFG) construction, function signature identification, and most of the binary static analyses.

Popular static disassemblers and binary analysis tools [9, 15, 17, 21, 24, 27, 28, 42, 48, 55, 63, 65] can use the *linear sweep* or the *recursive traversal* algorithm combined with various architecture-specific heuristics to disassemble binaries [6, 52]. However, accurate disassembly is difficult. The compiler settings and the complexity of instruction set architectures (ISAs) pose challenges to disassembly. Moreover, even the most advanced disassembly efforts experience difficulties from missing symbols and high-level data types, embedded data in code, and especially obfuscation. Typical frameworks (e.g., [27, 42]) place emphasis on precise disassembly and can miss a considerable set of function boundaries when the instructions of obfuscated binaries are improperly disassembled.

Machine-learning-based disassembly involves locating function entries [9, 53], recovering debugging information [26], differentiating code from data [14, 67], and identifying assembly instructions [46, 69]. Identifying function boundaries is challenging for stripped binaries due to the lack of symbols. Existing efforts use the weighted tree structure to learn the signatures of function starts [9] or the recurrent neural network (RNN) model to predict the function boundary [53]. Despite the systematic evaluation [34] demonstrating that such learning-based function identifications do not necessarily outperform the rule-based approaches [7, 27, 42], the deep learning technique has an advantage in unifying the function and instruction boundary recovery. For example, the bidirectional RNN model [53] has been extended by [46] to identify the instruction boundaries, and XDA [46] uses the BERT model [31] to solve the two disassembly tasks by transferring the knowledge of code bytes' dependencies.

The deep-learning based disassembly approaches [46, 53, 69] are proven to be more robust than the traditional disassembly frameworks [27, 42]. The deep-learning based approaches are further classified into two categories:

- (1) *Code-byte classification* [46, 53] differentiates the function- or instruction-boundary bytes from the non-boundary bytes. The deep models of these classifications, e.g., bidirectional RNN [53] and BERT [46], learn the byte-level correlations completely from the raw code bytes and thus are adaptive to different ISAs.
- (2) *Superset-instruction classification* [69] identifies true (or function-entry) instructions. This approach abstracts high-level features from a set of possible instructions using superset disassembly [11] and uses the relational graph convolutional network (R-GCN) model to classify instructions.

These approaches have their respective merit in accuracy or efficiency. However, none of them was designed with the consideration

*Both authors contributed equally to this research.

†Co-corresponding authors.

of facilitating an accurate binary-level CFG generation, where the major challenge is to resolve the precise indirect call target.

Goals. The code-byte classification approach can avoid the superset disassembly procedure. However, using superset disassembly as a feature-preparation step can enrich the features of the deep model with high-level knowledge. Moreover, superset disassembly relies on decoding and thus excludes erroneously decoded bytes from being predicted by the deep model. Such unnecessary predictions cannot be avoided in the code-byte classifications. On the other hand, the code-byte classification models are more straightforward to develop than the R-GCN model [69], which requires complicated static analysis to extract typed edges between instructions, build the instruction flow graph, and adapt the graph representation to the lightweight deep model. Besides, the deep models' obfuscation resilience capability is inadequately evaluated, mainly over the binaries obfuscated with Hikari [70], i.e., a deprecated descendant of Obfuscator-LLVM [2, 29], and limited to individual obfuscation options.

Therefore, our first research objective is to develop a new deep-learning based disassembly framework that takes the best of both sides to use the high-level knowledge of superset instructions and rely on simple features to learn instruction correlations. The new deep model should apply to multiple disassembly tasks and be resilient to more obfuscation techniques, e.g., disassembly desynchronization [4, 30] and advanced source-level obfuscation [20].

Beyond identifying function entry-points and assembly instructions, control flow graph (CFG) recovery is another crucial step of disassembly, which is challenging due to the existence of indirect calls. Reversing binary-level constructs to source-level data types can help resolve the targets of indirect calls and is also important for various binary analyses [26, 39, 45]. In particular, reversed memory boundary information is critical for CFG recovery through a binary-level points-to analysis [32, 33]. Moreover, memory boundary information is beneficial for hardening and securing binary code, e.g., vulnerability identification and mitigation [56, 60, 64] and memory sanitization for fuzzing [19]. However, existing approaches for recovering the boundary information rely on conservative heuristics, which can cause inaccurate downstream analysis. Thus, our second research objective is to employ deep learning to recover memory boundary information. Towards this objective, our key observation is that boundary information can be inferred by a value-tracking analysis over boundary-related instructions; further, classifying boundary-related instructions aligns well with deep learning. In this way, CFG recovery is reduced to the problem of detecting boundary-related instructions.

Method. In this work, we propose a new learning-based disassembly approach called DISA. It targets three disassembly tasks: T_1) function entry-point identification, T_2) true instruction identification, and T_3) memory block boundary identification for improving CFG recovery. The three tasks are conducted independently of each other using different deep models that share a homogeneous model architecture. The first step of DISA is the superset disassembly, which decodes the bytes at each possible code address to derive the information of the overlapping superset of potential instructions. DISA uses the information of decoded instructions over the multi-head self-attention to learn the instructions' correlations in these task scenarios. Benefiting from the high-level knowledge of

superset instructions and the encoder's capability of discovering long-range dependencies, DISA has an outstanding performance in disassembling binaries obfuscated by [20, 30].

Besides identifying true instructions and function-entry instructions, DISA has another capability of identifying memory block boundaries. DISA's instruction representation and embedding are appropriate for classifying instructions instead of instruction operands. As a disassembly framework that predicts superset instructions, DISA's deep model first classifies memory-accessing superset instructions to identify instructions that manipulate block-boundary data elements, i.e., block-boundary-related (*BRel*) instructions. Then, DISA uses a post-classification value-tracking procedure to translate the decision of *BRel* instructions into valid memory block boundaries. Our design of the bidirectional value-tracking analysis makes deep-learning based disassembly approaches applicable to memory block boundary identification, which is critical to downstream applications such as binary-level points-to analysis and CFG recovery. By integrating the results of the tasks into the block-memory model based points-to analysis (BPA) [32], DISA makes a novel combination of deep models and static analysis to resolve indirect call targets and construct accurate, assembly-level CFGs. The self-attention mechanism of DISA's deep model can efficiently learn the code features and ease the labor of static analysis as used by related approaches [26, 39, 69].

Evaluation. Our evaluations on tasks T_1 and T_2 are focused on the accuracy, robustness, and efficiency of DISA compared with the state-of-the-art learning-based disassembly approaches [46, 53, 69] and traditional frameworks [27, 42]. After evaluating the accuracy of the best deep models we can obtain, we demonstrate DISA's generalizability over real-world programs, using binaries built with complex optimization options discovered by BinTuner [49], and the binaries obfuscated with Obfuscator-LLVM, desync-cc, tigress, VMProtect, and Themida. Our investigations use more obfuscators and more intensive obfuscation options than previous work [46, 69], combined with different compiler optimization levels, demonstrating DISA's efficacy in real-world obfuscation. Besides, we also build more fine-grained deep models with x64-ELF binaries to investigate their capability to generalize to obfuscated binaries. Efficiency evaluation on obfuscated binaries shows that DISA outperforms XDA and Ghidra and is competitive with other approaches. For evaluating task T_3 , we demonstrate that the DISA-based improvement of BPA outperforms the original BPA, approximating the performance of the reference BPA using block boundary ground truths for the points-to analysis. Additionally, the ablation study shows that BPA with DISA is more effective in recovering the CFG when all DISA tasks, i.e., T_1 , T_2 , and T_3 , are included.

Contributions. We make the following contributions.

- (1) DISA outperforms SOTA classification approaches [46, 53, 69] on the robustness in disassembling binaries obfuscated with the disassembly desynchronization technique [30] and identifying function entries of binaries obfuscated with advanced source-level obfuscation technique [20]. Specifically, DISA improves the SOTA function entry-point identifications by 9.1% against [30] and 13.2% against [20].
- (2) DISA is the first disassembly approach that can identify memory block boundaries at the binary level. Unlike the learning-based binary data type inference approaches, DISA simplifies

the prediction of complicated instruction operands into the determination of block-boundary-related instructions with a value-tracking analysis. Disa excels in memory block boundary identification, outperforming BPA by 18.5% in precision, 11.6% in recall, and 16.1% in F1-score. In particular, when it comes to local memory block partitioning, Disa surpasses BPA with 27%, 21.3%, and 24% in precision, recall, and F1-score, respectively.

- (3) We improve BPA [32] by integrating Disa. By replacing BPA's heuristics-based memory blocks with Disa's more precise memory blocks, we achieve a 4.4% reduction in AICT and demonstrate the potential to offer more precise CFGs, better suited for downstream security applications. As a result, Disa and Disa-facilitated BPA achieve the assembly-level accurate CFG construction from the raw binary. Disa's implementation is publicly available at <https://github.com/peicwang/Disa>.

2 Background

2.1 Scope of Disa

Locating function entry-points, identifying assembly instructions, and recovering binary-level CFG are the three primary steps of static binary disassembly. Disa is designed to focus on such primary steps. These primary steps are relied upon by more advanced reverse-engineering steps [6, 43] such as symbolization and recovering function signatures. There are two major types of CFG recovery methodologies: signature matching and points-to analysis. We craft Disa to help improve the block-memory model based points-to analysis (BPA) [32] by identifying memory-block boundary related instructions, since BPA is the most practical points-to analysis for CFG recovery in terms of accuracy and efficiency. More background on CFG recovery can be found in Section 2.2. Moreover, memory blocks can be of different granularity. For example, one can design a points-to analysis to accommodate compound memory blocks (i.e., a group of memory blocks as one super block). In theory, Disa can be applied to generate compound memory blocks, as long as the ground-truth data for training contains compound memory blocks. However, in this paper, we limit our scope to memory blocks corresponding to BPA's definition. In other words, one memory block should be one continuous range of memory locations, mapping to one source-level compound data structure. Thus, memory blocks in our discussion can be perfectly identified by source code or debugging information. The Disa improvement of BPA (i.e., BPA_{Disa} in Section 4) is compared in CFG recovery effectiveness with the original BPA and a reference version of BPA (i.e., BPA_{DWARF} in Section 5.2) which uses the DWARF-based memory block ground truths to resolve indirect branches. Comparing BPA_{Disa} with signature matching based CFG recovery is out of our scope since they do not rely on memory blocks and our comparison is meant to show the effectiveness of Disa's memory block prediction.

Disa focuses on static disassembly on stripped x86/x64 binaries. Moreover, Disa's function entry and instruction identifications accommodate binaries obfuscated by several source-level obfuscators, i.e., Obfuscator-LLVM, desync-cc, and tigress. Especially, the disassembly desynchronization implemented by [30] uses opaque predicates to trick disassemblers into decoding the machine-code sequence at wrong offsets, which potentially yields valid albeit meaningless assembly code. Such obfuscation features are captured

by deep-learning based disassemblers like Disa but pose a significant obstacle to traditional frameworks. The static disassemblers like Disa can hardly disassemble dynamically generated code or runtime code decryption. Several assembly-level obfuscators, e.g., VMProtect [57] and Themida [59], intensively rely on these techniques to hide code. Our evaluation in Section 5 reports the static disassemblers' limited capability over a large part of the runtime-reached code produced by these obfuscators. Since the binary-level points-to analyses, e.g., BPA, Value-Set Analysis, and Disa's post-classification value tracking, have yet accommodated obfuscated binaries, Disa generates assembly-level CFG on obfuscated binaries without resolving indirect edges, even though Disa's deep model has a good potential to predict the *BRel* instructions of these binaries. Incorporating dynamic techniques, e.g., [10, 16, 22] is left for future work.

2.2 Control Flow Graph Recovery

Control flow graph (CFG) recovery from binary is one important step of disassembly, where the most challenging task is to decide the indirect call edges. However, the SOTA superset-disassembly based CFG recovery either omits indirect calls [12, 23, 35, 40, 66], or converts the indirect branch resolving into a rewriting-based mapping lookup [11]. During runtime, indirect calls can target different functions at different times. Thus, our task is to find a set of functions as the possible targets of each indirect callsite. Typical approaches include points-to analysis (e.g., Value-Set Analysis (VSA) [8] and BPA [32]) and signature matching methods (e.g., TypeArmor [61] and rCFI [41]). Among these techniques, points-to analysis can achieve the best accuracy of CFG recovery from stripped binaries. Note that inferring data types and data structures can further improve the accuracy of indirect call edges [18, 38, 71]. In addition to classic program-analysis based approaches, recent efforts [72] [58] have used deep neural networks to predict indirect call edges by transferring knowledge of direct calls' contexts. The scope of usage of these works differs from our general-purpose disassembly framework.

2.3 Memory Block Generation of BPA

Points-to analysis is fundamental for recovering CFGs of stripped binaries. VSA and VSA variations, however, are too expensive to scale. In contrast, BPA [32] implements points-to analysis based on a *block memory model*, the key to achieving both scalability and precision. In this memory model, the memory is modeled as a set of disjoint *memory blocks*. Each block is comprised of a logically cohesive set of memory locations. For example, the stack of a function can be divided into a set of memory blocks, with one block for each local variable. All locations in a block are treated as equivalent during points-to analysis; that is, any read/write to a location in a block is treated as operating on all locations in the block. By using memory blocks, BPA avoids reasoning about pointer arithmetics; specifically, the block memory model assumes that it is not possible to make a pointer to one block point to a different block via pointer arithmetics. BPA takes advantage of this to achieve much better scalability than VSA.

The accuracy of memory block boundaries, however, becomes one deciding factor for BPA's points-to analysis. Coarse-grained

boundaries are more scalable, but result in less precision. An accurate memory block is defined as a set of memory locations that correspond to some source-level compound data structure. BPA uses heuristics to generate memory blocks, with the principle that any pointer arithmetic needs to stay within a block. More details of BPA's memory block generation can be found in the paper [32].

BPA's manually designed heuristics can be either too conservative or too aggressive, causing many false positives or false negatives. Therefore, DISA's task T_3 is designed to obtain accurate memory block boundaries by deep learning, so that the block-memory model based points-to analysis such as BPA can achieve better accuracy in recovering CFGs. As a result, DISA is the first work that extends deep learning from function entry and instruction identification to accurate CFG construction, while other deep-learning-based approaches [46, 53, 69] only focus on the first two tasks of DISA.

3 Design of DISA

The workflow of DISA is presented in Fig. 1. DISA has three disassembly tasks: function entry-point identification (T_1), true instruction identification (T_2), and memory block boundary identification (T_3). For each task, DISA adopts a deep neural network model, which makes binary classification on instructions resulting from superset disassembly. The model of task T_1 classifies function entry-point instructions; the model of task T_2 determines whether a superset-disassembly instruction is a true instruction; and the model of task T_3 identifies *block-boundary-related (BRel) instructions*. A *block-boundary-related instruction* is a true instruction that accesses a memory block boundary address. An instruction may access multiple memory addresses in different executions, e.g., an instruction in a loop. In that case, the instruction is *BRel* instruction if at least one of these memory addresses is a block boundary address. Then, we use a static boundary recovery procedure to transform T_3 's prediction results into memory block boundaries. As a security application, the block boundaries recovered from T_3 's prediction results are delivered to BPA to predict the targets of indirect calls. We call the integrated system, BPA_{DISA} . In addition, the prediction results of T_1 and T_2 are provided to BPA_{DISA} for the integration of three DISA tasks, resulting in BPA_{DISA}^{T12} .

DISA implements two decode primitives over the results of superset disassembly to extract all the instruction fields used in the learning-based disassembly tasks. Differently from the fields used by [69], we use more high-level knowledge to infer the features of the manipulated data memory addresses from the superset instructions for task T_3 . Therefore, our decode primitive extracts the *memory region* and *relative displacement* information from memory-access instructions, in combination with other addressing fields to decide the *BRel* instructions (Section 3.1). The key component of our deep model is the encoder structure of the transformer. For each disassembly task, the encoder's multi-head self-attention mechanism learns the relevances among the superset instructions, predicts valid instruction sequence patterns through a binary classification, and finally derives the function entries, true instructions, or *BRel* instructions (Section 3.2). We then use intra-procedural value tracking analysis to recover the memory block boundaries for BPA_{DISA} from the outputs of T_3 's deep model (Section 3.3).

3.1 Extracting Instruction Information

Decoding instructions from raw bytes at each offset of the code section of an input binary is guaranteed to obtain a superset of true instructions. This superset disassembly [11] causes no instruction-level false negatives, thus reducing the disassembly task into an instruction classification problem on the superset. Although the instruction superset is not essential to a deep-learning-based disassembly (e.g., one can do raw-byte classification as in XDA), we take the superset disassembly as the first step to obtain the knowledge of instructions, as performed by [68, 69]. For a code byte vector $b_{0..S-1}$, we obtain the superset $SI = \{ins_i \mid ins_i \leftarrow decode(b, i), 0 \leq i < S\}$. $decode(b, i)$ linearly disassembles the bytes at the offset i and returns an assembly instruction or a decoding failure. Since decoding may fail, SI generally can have less than S instructions, ordered by their offsets from the start of the code section.

Conceptually, a decoding primitive $decode(b, i)$ takes a sequence of bytes and outputs all information about the instruction encoded by the bytes. Practically, we extract only necessary information from the decoded instruction. Representing the instruction as text tokens, e.g., [36], would cause an enormous dictionary and inefficient model training procedure. Instead, we define two decoding primitives to extract typical fields from each instruction and map the value of these fields as integers for model training:

$$\begin{aligned} decode_1(b, i) &= (Op_i, ModRM_i, SIB_i) \\ decode_2(b, i) &= (Op_i, ModRM_i, SIB_i, Disp_i, Rgn_i) \end{aligned}$$

For the models of function entry and instruction identification, $decode_1$ extracts *Opcode*, *ModRM*, and *SIB*¹ from an instruction. The three fields are encoded into disjoint integer ranges, ensuring each possible value of the three fields has unambiguous meaning. Thus, $decode_1$ outputs a triple of integers as the representation of the instruction. For robustness, we do not use any instruction prefix.

Memory block boundaries are related to data operations over compound data structures. A stack memory block boundary can be represented as an offset from the stack pointer (esp) at the function's entry. A global memory block boundary is an offset from the start of global sections (.data, .rodata, .bss). For task T_3 , $decode_2$ extracts more information to represent the feature of memory operations on the global and stack data structures. Firstly, T_3 is concerned with only memory-access instructions and branching instructions. Other instructions are not decoded in task T_3 . Instead of applying complex analyses over instructions [69], we use a simple, per-instruction memory-access knowledge extraction.

Specifically, we derive a *memory region (Rgn)* and a *relative displacement (Disp)* as auxiliary memory access features. An instruction's *Rgn* is an integer encoding a region from

$$\{\text{heap, stack, rodata, data, bss, unknown}\},$$

indicating where the memory block manipulated by the instruction is located. We use heuristic-based pattern matching to decide the *Rgn* value of each instruction. These patterns include specific registers, constant values, and whether the constants fall in specific global sections, which are computed by the instruction's *ModRM*,

¹The *ModRM* byte specifies the addressing mode and register combination for the instruction. The *Scale-Index-Base (SIB)* byte follows the *ModRM* byte to represent more flexible addressing memory operands.

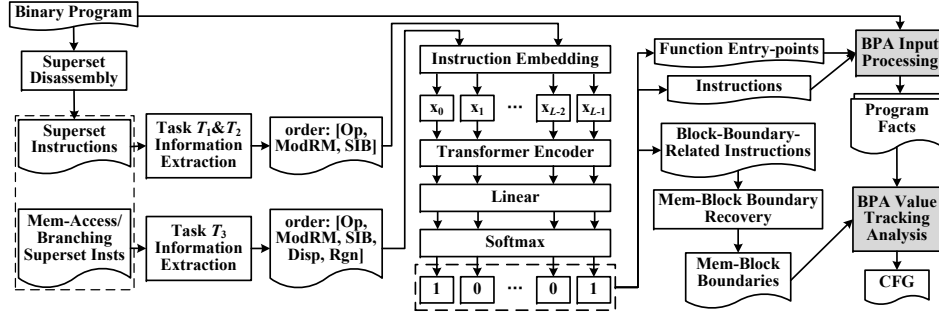


Figure 1: Workflow of Disa

```

struct discard_rule {
    void (*condition)();
    int flag;
} rules[] = {{fptr1, 0}, {fptr2, 1}, {fptr3, -1}};
void discard_moves() { int i, user_f;
    for(i=0; i<3; ++i) {
        rules[i].condition();
        user_f = rules[i].flag;
    }
    rules[2].condition(); ...
}

```

<discard_moves>	[Ord]	[Inst]	[Rgn]	[Disp]	[BRel]
319:	mov	[ebp - 0xc]4, 0	(stack, -12)		X
322:	add	[eax]1, al	(unkn., \perp)		
323:	add	[eax]1, al	(unkn., \perp)		
324:	add	[eax]1, al	(unkn., \perp)		
326:	jmp	356	(unkn., \perp)		
328:	mov	eax, [ebp - 0xc]4	(stack, -12)		X
331:	mov	eax, [eax*8 + 0x804a018]4	(data, 8)		X
333:	lds	ebx, [eax]2	(unkn., \perp)		
334:	sbb	[eax - 0x2f00f7fc]1, ah	(unkn., <-1024)		
335:	mov	al, [0xd0ff0804]1	(unkn., >1024)		
338:	call	eax	(unkn., \perp)		
339:	ror	[ebx + 0x48bf445]1, 1	(unkn., >1024)		
340:	mov	eax, [ebp - 0xc]4	(stack, -12)		X
343:	mov	eax, [eax*8 + 0x804a01c]4	(data, 12)		
345:	lds	ebx, [eax]2	(unkn., \perp)		
347:	mov	al, [0x45890804]1	(unkn., >1024)		
349:	or	[ecx + 0x45fff045]1, cl	(unkn., >1024)		
350:	mov	[ebp - 0x10]4, eax	(stack, -16)		X
352:	inc	[ebp - 0xc]4	(stack, -12)		
353:	inc	[ebp - 0xc]4	(stack, -12)		X
356:	cmp	[ebp - 0xc]4, 2	(stack, -12)		X
357:	jge	347	(unkn., \perp)		
359:	add	bh, [esi - 0x22]1	(unkn., -34)		
360:	jle	328	(unkn., \perp)		
361:	fisub	[ecx + 0x804a028]2	(data, 24)		
362:	mov	eax, [0x804a028]4	(data, 24)		
363:	...				

Not True Instruction True Branching Instruction

Figure 2: Example with Auxiliary Features and *BRel* Instructions (upper=lower=1024, .data is [0x804a010, 0x804a02f]).

SIB, and *Displacement*². If we cannot track the region of a memory-access expression during the instruction-decoding procedure, *Rgn* is labeled unknown.

The instruction's relative displacement *Disp* is the offset from a base addressing expression in the data sections or a stack frame. For encoding convenience, *Disp* can differ from *Displacement*. For examples in Fig. 2, the *Displacement* 0x804a018 of instruction 331 has the corresponding *Disp* 8 because 0x804a018 falls into the .data section [0x804a010, 0x804a02f], while for instruction 319, the *Displacement* (-0xc) is an offset and identical to the *Disp* (-12). The representation of *Disp* leads to an integer encoding of { \perp , <lower, lower, ..., upper, >upper}, where \perp means the absence of *Displacement*. [lower, upper] is a fixed range of consecutive integers that

²*Displacement* specifies a static (uncomputed) address or offset for addressing.

represent those exact relative displacements tracked by our model, e.g., from -1024 to 1024. This range is selected to not intersect with \perp , <lower, >upper, *Opcode*, *ModRM*, *SIB*, and *Rgn*. The branching instruction positively impacts the decision of task *T3* instructions. To unify the instruction representation of task *T3*, the branching instructions are properly encoded with (*Rgn*, *Disp*)=(unknown, \perp). As a result, *decode*₂ returns a quintuple of integers to represent each memory-access or branching superset instruction.

For an example adapted from gobmk of SPEC2k6, Fig. 2 presents the superset memory-access and branching instructions of the function *discard_moves*. Decoding failures are not presented. We deem that the memory-access patterns of instructions reflect the boundary features of compound data structures. The labels of *BRel* instructions are derived from the ground truth, as described in Section 3.3. Task *T3*'s model training uses these labels but does not use the information about true instructions; thus, tasks *T3* and *T2* are independent. For simplicity, Fig. 2 elides the results of *Opcode*, *ModRM*, and *SIB* and includes only (*Rgn*, *Disp*). As shown in the figure, the decoded quintuples of true *BRel* instructions differ in pattern from the block-boundary-unrelated memory-access instructions. In the example, an instruction within unknown region tends to be predicted as not a block-boundary instruction. The local variables *i* and *user_f* respectively locate at [ebp-0xc]4 and [ebp-0x10]4. Their boundaries are memory block boundary thus the true instructions accessing them, i.e., instructions at 319, 328, 340, 350, 353, and 356, are *BRel* instructions. Considering the global compound data structure rules, rules[0] starting at 0x804a018 with (*Rgn*, *Disp*)=(data, 8) is a memory block boundary, and the instruction accessing the global region at 331 is a *BRel* instruction. In contrast, the instructions 343 and 362 respectively access rules[i].flag and rules[2]. The global addresses touched by these instructions are not memory block boundary because there are pointer arithmetics crossing these addresses. Differentiating the *BRel* instruction 331 from the block-boundary-unrelated instructions (343 and 362) with similar (*Rgn*, *Disp*) pairs requires more context knowledge. Our deep model learns the correlations among the contexting quintuples of the memory-access and branching instructions to correctly predict these instructions. The knowledge of branching instructions, either true (326, 338, and 360 of Fig. 2) or not true (357 of Fig. 2), also helps classify the *BRel* instructions.

3.2 Instruction Embedding and Self-Attention

The instruction fields and position are both critical knowledge for disassembly. Each superset instruction's position is critical to reflect

the context of the instruction in the final disassembly code. For example, a conditional branch instruction following `cmp` is more likely than other kinds of instructions. Therefore, DISA's instruction embedding consists of *instruction position embedding* and *instruction fields embedding*.

Modeling the relevances of all N instructions in the superset SI for classification would be costly and unnecessary for disassembly. Instead, we use a smaller, constant-length input sequence with length L to embed the superset instructions. The superset instructions of a binary are separated into $\lceil N/L \rceil$ input sequences, and the last input sequence would be padded in tail with a particular padding integer. Each element of the input sequence is indexed from 0 to $L - 1$, indicating the relative position. A learned embedding layer takes the indices as input to embed the relative instruction positions. The output indicates all the position information of the instruction sequence. For the instruction fields embedding, the fields of each triple of T_1 and T_2 are respectively embedded with three learned embedding layers. We concatenate the three embeddings to form the instruction fields embedding with dimension d_{model} [62]. Similarly, for the integer quintuple of each instruction in T_3 , we use an embedding layer for each field and concatenate the five embeddings into an instruction fields embedding. Adding each dimension of the position and fields embedding derives the final instruction embedding of the instruction sequence.

DISA uses the encoder structure of the transformer [62] to classify superset instructions. Each layer of the encoder iteratively updates the instruction embedding of the instruction sequence and derives the representations capturing the patterns of true function entries or (*BRel*) instructions. The output embeddings of the encoder are delivered to a linear and a softmax layer to predict the probability of the verdict on each superset instruction. Because DISA's deep model learns the relevances among superset instructions from the binary labeling on instructions, our model can use the instructions' relevance knowledge to determine the binary classification by predicting the binary labeling patterns. The capability of the encoder structure to learn the high-level semantic relevance of superset instructions makes DISA's model more effective and robust than the raw-byte based deep models [46, 53] and the R-GCN model [69], which requires complex prior-static analysis on task T_2 ; as a result, DISA is easier to develop than the R-GCN model [69].

3.3 Memory Block Boundary Recovery

Task T_3 uses a deep-learning model to identify instructions that access memory-block boundary addresses. The model's prediction results are about which instructions are boundary-related instructions and are not directly usable for systems such as BPA, which requires memory block boundary information. To fill in the gap, we devise a follow-up static analysis to recover memory block boundaries from task T_3 's results. Next we discuss this static analysis and after that we will elaborate on the process of generating the ground truth for T_3 's model training in Section 3.3.1.

The static analysis is an intra-procedural value tracking analysis, which we call *boundary-targeted value tracking analysis* (bVTR). This analysis is conducted to convert the memory operands of instructions into memory block boundaries, i.e., as offsets from a function F_i 's entry value of esp or some global region.

The primary logic of bVTR revolves around the value set analysis, as sketched in Algorithm 1. The bVTR algorithm takes as input the binary file and the predicted *BRel* instruction addresses provided by DISA T_3 . The output of the analysis is a set of pairs ($Rgn, MemBlocks$), where Rgn is a global region such as `.rodata`, `.bss`, `.data`, or a function name for the function's stack, and $MemBlocks$ is the memory block boundaries of Rgn . In order to determine the final memory block boundaries, the bVTR invokes the *FuncWiseVSA* procedure for each function in the binary to calculate instruction-level *ValueSets*. In general, a value set tells the set of possible values of a register or a stack slot. For a pointer to the stack, it tracks the set of possible offsets to the initial esp value at the function entry. For example, after instruction 313 (a push instruction) in Fig. 3, esp's offset to the initial esp value is -4; after instruction 314, ebp's offset to the initial esp value is also -4.

Algorithm 1: Boundary-Targeted Value Tracking

Input: Binary file, DISA T_3 predictions
Output: ($Rgn, MemBlocks$)

```

1 foreach function in the binary do
    // Conducts VSA and returns value sets for each instruction
2   ValueSets  $\leftarrow$  FuncWiseVSA(disasmFunc);
    // Returns region-wise memory blocks
3   ( $Rgn, MemBlocks$ )  $\leftarrow$ 
      GetMemBlocksFromDISA(ValueSets,  $T_3$  predictions);

```

After the function-level value-set analysis, *GetMemBlocksFromDISA* processes each predicted *BRel* instruction by referencing and simplifying the memory operand using its computed *ValueSets* result to derive the final *Memblocks*. Since only those boundary-related instructions are supposed to access memory block boundaries, using those operands' value set results would produce the boundaries of memory blocks. For example, at instruction 319 in Fig. 3, we derive the value of operand `ebp-12` with ebp's current value set and obtain `(-16)@discard_moves` as a valid boundary. Note that our algorithm tracks the values in global sections, though we ignore them in Fig. 3 for simplicity.

GetMemBlocksFromDISA may derive multiple block boundaries from one instruction; e.g., on instruction 331, we obtain three boundaries `{8, 16, 24}@data` due to three possible values of `eax`. Our instruction-level prediction prohibits DISA from differentiating these boundaries if only part of them are real boundaries: if one instruction touches both true and false block boundaries, our algorithm labels such an instruction as *BRel*, and our system could introduce false-positive block boundaries. For example, even though `24@data` is not a true memory boundary due to the *BRel* label at 362 and DISA's T_3 model can make the correct prediction, such global address will still be decided as block boundary by bVTR over instruction 331. Besides, due to the potential imprecision of the value tracking, e.g., heap values are ignored, Task T_3 's prediction may result in having an offset on the unknown region. In that case, we deem this offset not a memory block boundary.

3.3.1 Ground Truth Collection for T_3 Model Training. The ground truth collection for T_3 consists of two parts. The first involves extracting memory block boundaries from DWARF information. The second entails using these extracted boundaries to obtain ground truths for training T_3 's deep model, i.e., those *BRel* instructions.

[Ord]: [Inst]	[BRel]	(ebp, esp, eax, stk _{{-16,-12}, stk_{-20,-16})}	[Bound Comput.]
<discard_moves>:		{}, {0}, {}	
313: push ebp		{}, {-4}, {}	
314: mov ebp, esp		{-4}, {-4}, {}	
316: sub esp, 0x18		{-4}, {-28}, {}	
319: mov [ebp - 0xc]4, 0	X	{-4}, {-28}, {}, {0}	ebp - 12 = (-16)@discard_moves
326: jmp 356 <313+0x2b>			
328: mov eax, [ebp - 0xc]4	X	{-4}, {-28}, {0,1,2}, {0,1,2}, {}	ebp - 12 = (-16)@discard_moves
331: mov eax, [eax*8 + 0x804a018]4	X	{-4}, {-28}, {}, {0,1,2}, {}	eax*8 + 0x804a018 = {8,16,24}@data
338: call eax		{-4}, {-28}, {}, {0,1,2}, {}	
340: mov eax, [ebp - 0xc]4	X	{-4}, {-28}, {0,1,2}, {0,1,2}, {}	ebp - 12 = (-16)@discard_moves
343: mov eax, [eax*8 + 0x804a01c]4		{-4}, {-28}, {}, {0,1,2}, {}	
350: mov [ebp - 0x10]4, eax	X	{-4}, {-28}, {}, {0,1,2}, {}	ebp - 16 = (-20)@discard_moves
353: inc [ebp - 0xc]4	X	{-4}, {-28}, {}, {0,1,2,3}, {}	ebp - 12 = (-16)@discard_moves
356: cmp [ebp - 0xc]4, 2	X	{-4}, {-28}, {}, {0,1,2,3}, {}	ebp - 12 = (-16)@discard_moves
360: jle 328 <313+0xf>		{-4}, {-28}, {}, {0,1,2,3}, {}	
362: mov eax, [0x804a028]4		{-4}, {-28}, {}, {0,1,2,3}, {}	
367: ...			

Figure 3: Value Tracking with Boundary Identification

```

101: 8d 4c 24 04    lea    ecx, [esp+0x4]
102: 83 e4 f0       and    esp, 0xfffffffff0
103: ff 71 fc       push   DWORD PTR [ecx-0x4]
104: 55            push   ebp
105: 89 e5          mov    ebp, esp
106: 53            push   ebx
107: 51            push   ecx
108: 83 ec 20       sub    esp, 0x20

```

Figure 4: Sample Function Prologue

```

DW_TAG_variable
DW_AT_name      ("array1")
DW_AT_type      (0x0000034a "int[5]")
DW_AT_location  (DW_OP_breg5 EBP-32)

```

Figure 5: Sample DWARF for a Variable

Extracting Block Boundaries. DWARF [1] is a debugging information format that encodes source-code information in binary code. The DWARF debugging information is a series of debugging information entries (DIEs) such as data types and locations of variables, arrays, and other complex data structures. Since debugging information is needed by generic debuggers, compilers need to produce debugging information with high precision, even if optimizations are turned on. The type information and location information inside the debugging information can help determine the boundaries of memory blocks. For example, if the debugging information tells that the first element of an array of 10 bytes resides in memory address 1000, we can infer that the memory block that represents the array has the range [1000, 1009]. Assuming that pointer arithmetic should not cross the boundary of source-level data structures, memory blocks extracted from debugging information can be treated as ground truth.

We extract debugging information entries (DIEs) for variables, functions, and location tags, equivalent to DWARF representations of DW_TAG_Variable, DW_TAG_Subprogram, and DW_AT_location, respectively. Subsequently, these entries are processed to yield output formatted as (*Rgn, offsets*). The *offsets* denote the list of computed offsets from the beginning of a global region or, for the stack, from the initial esp of a function. Notably, DWARF provides stack location information in various forms, such as base registers like ebp/esp or call frame base, coupled with a displacement value. Changes in the relationship between these base registers and the function’s starting esp may occur based on different optimizations. To address this, we perform a function prologue analysis to standardize the debugging information into our format, ensuring alignment of every offset with the initial esp.

For example, a sample function prologue is presented in Fig. 4. A close inspection reveals the presence of two push operations at addresses 103 and 104, preceding the initialization of ebp with the value of esp. As a result, the distance between the initial esp and the ebp is determined to be 8 bytes, with each push operation consuming 4 bytes. Fig. 5 displays the DWARF information representing a variable denoted as array1. For brevity, other attributes of the variables are elided. The variable’s location is indicated using the DWARF tag DW_AT_location, offering the positional data as DW_OP_breg5 EBP-32. In the DWARF format for 32-bit x86 binaries, DW_OP_breg5 symbolizes ebp. The location data signifies the ebp base registers and an offset of -32. Since our output reflects the offset from the initial esp, adjusting the -32 by 8 allows us to ascertain that this memory block commences from an offset of -40 from the initial esp specifically for this function.

Identify Memory-Access Instructions. To accurately establish the required ground truth for DISA T_3 , we perform another value-tracking analysis, known as the *instruction-targeted value tracking analysis* (iVTR). Similar to bVTR, the key focus of iVTR is also the value set analysis. We extract the value sets for each assembly instruction and then compare them with the raw memory block offsets obtained with DWARF information. This approach enables us to pinpoint the memory addresses that access memory block boundaries.

Algorithm 2: Instruction-Targeted Value Tracking

Input: Binary file
Output: (*Rgn, instAddrs*)
// Extracts the raw memory blocks from DWARF
1 (*Rgn, offsets*) \leftarrow ExtBlkBndDWARF(binary);
2 **foreach** function in the binary **do**
 // Conducts VSA and returns value sets for each instruction
3 ValueSets \leftarrow FuncWiseVSA(funcName, binary);
 // Returns DISA task3 formatted ground truth
4 (*Rgn, instAddrs*) \leftarrow
 IdInstrTouchMem(ValueSets, (*Rgn, offsets*));

The iVTR algorithm in Algorithm 2 takes the binary itself as input and produces output in the form of (*Rgn, instAddrs*). *instAddrs* consists of the list of instruction addresses that interact with memory block boundaries, we label these memory-access instructions as *BRel*. In the first step, iVTR calls the ExtBlkBndDWARF function, which processes the binary and returns the raw offsets in the format of (*Rgn, offsets*). Subsequently, for each identified function in

the binary, we execute FuncWiseVSA to obtain the instruction-wise ValueSets. After obtaining the ValueSets for each instruction, the IdInstrTouchMem procedure iterates over all instructions in a function and detects instructions that touch global or stack memory. Then it cross-references them with the previously generated ValueSets and the DWARF based (*Rgn, offsets*) to mark *BRel* instructions and place those instruction addresses at *instAddrs*. Upon acquiring the result of iVTR, we proceed to generate the complete ground truths to train the deep model of Task T_3 , which is used to predict *BRel* instructions for unknown binaries and to recover memory block boundaries with Algorithm 1.

4 Implementation

We implemented Disa with PyTorch [44]. We used Capstone 5.0.1 [47] to decode instructions. To accelerate this procedure, we used the C language API of Capstone [3] to implement a multi-thread superset disassembly and instruction fields extraction procedure. To implement Disa's T_3 , our initial approach involved using Angr [54] to develop bVTR and iVTR algorithms. However, we encountered limitations with Angr's default support for instruction-level granularity, leading us to modifying Angr's source code to obtain instruction-level value set information. However, this Angr-based implementation was time- and resource-intensive; so we resorted to developing a Datalog-based lightweight value set analysis. This approach was combined with Python scripts to implement bVTR and iVTR algorithms. To integrate Disa into BPA, we removed BPA's heuristic-based memory block generation step. We used the bVTR procedure to convert the prediction results of Disa's T_3 model into addressing values/offsets in specific memory regions. Such memory block boundaries were fed as input to the following steps of BPA. Finally, we obtained the Disa-facilitated BPA, i.e., BPA_{Disa} .

We use 1,794 integers to encode the *Opcod* field, including two integers for the Intel CET instructions ENDBR32 and ENDBR64, and 768 integers for encoding VEX opcodes commonly seen in ICC binaries. *ModRM* has 257 cases, in which one case represents the absence of *ModRM*. Similarly, *SIB* has 257 cases and one case represents *SIB*'s absence. In our implementation, The length of input sequences is $L = 512$, and the dimension of inputs to the transformer's encoders is $d_{model} = 384$. Our model has 6 encoder layers and 8 attention heads. Compared with XDA [46] (i.e., #head= 12, #encoder-layer= 12, $d_{model} = 768$), our deep model is much simpler (Table 6). Disa's batch size is 16. We observed class imbalance during the training procedure of our disassembly tasks, especially in the function entry-point identification. Thus, we use the α -balanced variant of Focal Loss [37] as the loss function to ensure the training procedure focuses more on the sparse positive samples.

5 Evaluation

Our evaluations aim to answer the following research questions:

- RQ1. How accurate is Disa in identifying function entries and instructions compared with existing approaches?
- RQ2. How robust is Disa on unseen and obfuscated binaries?
- RQ3. How effective is Disa in deciding the memory block boundaries? How secure can Disa achieve for BPA_{Disa} 's forward-edge resolving?
- RQ4. How efficient is Disa compared with existing approaches?

Table 1: Datasets

Dataset	Compiler	Origin	#Binary	#Inst Seq.	
SN	SN ^{x86} _{ELF}	GCC-9.2, GCC-4.7.2	SPEC2k6&2017+BAP [*]	731	510,527
		Clang-14.0	SPEC2k6&2017	215	481,389
		ICC-2021.6.0, ICC-14.0.1	SPEC2k6&2017+BAP [*]	726	647,147
	SN ^{x64} _{ELF}	GCC-9.2, GCC-4.7.2	SPEC2k6&2017+BAP [*]	816	665,778
		Clang-14.0	SPEC2k6&2017	300	587,854
		ICC-2021.6.0, ICC-14.0.1	SPEC2k6&2017+BAP [*]	811	890,651
	SN ^{x86} _{PE}	MSVC-2022/2008	SPEC2k6&2017+LLVM11	341	1,093,236
	SN ^{x64} _{PE}	MSVC-2022/2008	SPEC2k6&2017+LLVM11	375	1,177,774
SR	SR ^{x64} _{ELF}	GCC	[69]	76	68,838
		GCC	Glibc-2.22 of [6]	1	2,187
	SR ^{BT} _{ELF}	GCC-9.4 with BinTuner	SQLite, thttpd, bzip2, diffutils	7	4,188
	SO	SO ^{DSY} _{ELF}	desync-cc on GCC-11.4	SPEC2k6&2017	99
SO ^{Oll} _{ELF}		ollvm on Clang-4.0.1	SPEC2k6&2017	100	867,894
SO ^{TIGR} _{PE}		tigress with GCC-14.1	crypto-algorithms	60	7,089
SO ^{VMP} _{PE}		VMProtect with GCC-14.1	crypto-algorithms	16	151,156
SO ^{MD5} _{PE}		Themida with GCC-14.1	crypto-algorithms	16	963
SP	SP ^{x86} _{train}	GCC-7.5	binutils, coreutils, [25]	2664	7,31,104
	SP ^{x86} _{test}	GCC-9.2	SPEC2k6	36	39,232

^{*} The binaries of BAP corpora are built with GCC-4.7.2 and ICC-14.0.1.

5.1 Dataset and Experimental Settings

The benchmark binaries consist of non-obfuscated binaries SN and SP, real-world binaries SR, and obfuscated binaries SO, as presented in Table 1. SN, SR, and SO are for tasks T_1 and T_2 , while SP is for task T_3 . We classify the benchmarks in SN based on the file format and ISA, e.g., SN^{x86}_{ELF}. The non-obfuscated binaries are from BAP corpora [17], LLVM11 for Windows³, or built from SPEC CPU 2006 and 2017 benchmarks with different compilers (GCC, Clang, ICC, and MSVC). We build the SPEC CPU benchmark binaries into x86 and x64 architectures on different optimization levels, i.e., 00-03 and 0s for GCC, Clang, and ICC; 0d, 01, 02, and 0x for MSVC. We deduplicate the length- L input sequences in each sub-dataset of SN to avoid the *train-test overlap* [46]. The numbers of input sequences after deduplication are in Table 1. SR comprises 76 real-world non-obfuscated binaries of 10 applications from [69], one shared object file Glibc-2.22 from [6], and another subset SR^{BT}_{ELF}. SR^{BT}_{ELF} has seven 01-03 binaries built with extremely complex optimization options obtained by setting the 00-binary as BinTuner's baseline. We build the obfuscated x64 binaries of SO on 00-03 with Obfuscator-LLVM [2, 29] (ollvm for short), desync-cc [4, 30], tigress [20], VMProtect [57], and Themida [59]. We apply tigress on the source code of cryptographic algorithms (e.g., DST40, SHA-256, XTEA, COMP128, MD5) and use GCC on MinGW to cross-compile the obfuscated PE binaries. We obfuscate the crypto-algorithm PE binaries cross-compiled by GCC on MinGW using VMProtect and Themida. We use the default option of desync-cc. We enable the `-sub`, `-fla`, `-bcf`, and `-split_num` options of ollvm simultaneously⁴. We use the options Flatten, EncodeArithmetic, and AddOpaque of tigress simultaneously. On average, the code section of the binary gets bloated by 5.78x with ollvm, 2.08x with desync-cc, and 25.33x with tigress. We use the binaries of binutils, coreutils, and MiBench [25] (SP^{x86}_{train}) to train Disa's T_3 model and the SPEC2k6 binaries on 00-03 as the testing dataset SP^{x86}_{test} to evaluate T_3 .

5.1.1 Ground Truths Preparation. The ground truths of SR^{x64}_{ELF} are from the related works [6, 69]. Here, we focus on the ground truths

³In this dataset, we use the binaries smaller than 5 MB. URL: <https://drive.google.com/file/d/1UfS4YsbKWw6Xlp7NXf4tTHDN7gzDRY7p>

⁴Our ollvm version does not support the option `indibran` as enabled by [46, 69].

of SN, SO, and SR_{ELF}^{BT} . We follow [69] to obtain the function entry ground truths of ELF binaries from the symbol table and symbol index using pyelftools [13]. The obfuscators on ELF do not strip the binaries after obfuscation, thus allowing this approach. For the SN_{PE} binaries, we use Dia2dump [5] to parse the PDB files and derive the function entries. For SO_{PE}^{TGR} , we use objdump to obtain the function entry ground truths from the symbol table. The function entry ground truths on SO_{PE}^{VMP} and SO_{PE}^{TMD} cannot be obtained without other deobfuscators; thus these datasets are used to evaluate T_2 . Like [46], we do not treat the thunks in PE binaries and the trampolines in the .plt section of ELF binaries as function entries. We also remove them from the analysis results to avoid mistaken false positives.

To obtain the instruction ground truth, we use linear disassembly with Capstone to obtain the ground truth of the GCC/Clang-built SN_{ELF} and SR_{ELF}^{BT} binaries because, according to [6], GCC and Clang never inline data into the code section. Overcoming the inaccuracy of Capstone’s per-instruction decoding is out of our scope. Capstone is a rational choice considering it is used by other frameworks, e.g., [46, 51, 68]. One can transfer to other decoders, e.g., [27, 73], as needed. ICC and MSVC introduce data, e.g., jump tables, into the code section. For the ICC-built SN_{ELF} binaries, we use IDA Pro’s API to locate the data slots in the code section. We manually confirm the slots that indeed hold data. Then, we exclude the data and use linear disassembly on the rest code sub-sections to obtain the true instructions. The parsing results of Dia2dump on SN_{PE} binaries contain the data addresses in the code section and labels. We follow [69] to exclude the data slots from the code section to obtain the ground truth. We treat NOP in ELF and INT3 in PE binaries as padding and do not count them as positive or negative.

The obfuscators are built on different compilers; thus, investigating the compiler-backend emitted assembly requires much effort. In contrast, we use a dynamic approach to obtain the sound but incomplete ground truths for the obfuscated binaries in SO. We developed a Pin tool to instrument the SO binaries and record the address and size of each runtime-reached instruction under standard workloads or typical test cases. Because the true instruction segments are separated by *unknown* slots that are unreachable at runtime, we treat a predicted instruction as positive if it overlaps at least one byte with a true instruction. Otherwise, this prediction is classified as unknown. We observed that over 50% of runtime-reached instructions of SO_{PE}^{VMP} binaries are in section .vmp1, while in SO_{PE}^{TMD} binaries, over 98% of the runtime-reached instructions are in section .themida. These sections contain the encrypted/compressed data or code that the static disassemblers cannot disassemble. We deem it a limitation of static disassemblers. As a result, in Section 5.4, we investigate the static disassemblers over section .vmp2 of SO_{PE}^{VMP} binaries and section .text of SO_{PE}^{TMD} binaries, which hold the static machine code whose ground truths can be obtained by our Pin tool.

To obtain the true memory block boundaries on SP_{train}^{x86} and SP_{test}^{x86} for T_3 , we follow the process in Section 3.3.1. We use pyelftools to extract the binary’s DWARF information and derive the raw memory block boundaries in both global sections and stack frames. The DWARF information is not directly suitable for our purposes, since we encounter location information missing particularly in cases where the location information includes complex DWARF

Table 2: Deep Models for Evaluations of RQ1 and RQ2

	Testing Dataset for Accuracy	Testing Dataset for Generalizability			
	SN_{test}^2	SR	SO		SN_{PE}
Model Name	XDA-SN	XDA-SN	XDA-SN	XDA- SN_{ELF}^{x64}	XDA- SN_{PE}^{x64}
	biRNN-SN	biRNN-SN	biRNN-SN	biRNN- SN_{ELF}^{x64}	biRNN- SN_{PE}^{x64}
	DEEPT _{ref}	DEEPT _{ref}	DEEPT _{ref}	N/A ¹	N/A ¹
	DISA-SN	DISA-SN	DISA-SN	DISA- SN_{ELF}^{x64}	DISA- SN_{PE}^{x64}

¹ DEEPT_{ref}’s reference model has the knowledge of x86 and PE binaries, thus we cannot compare its generalizability with the deep models trained only with the x64 ELF binaries (i.e., XDA- SN_{ELF}^{x64} /biRNN- SN_{ELF}^{x64} /DISA- SN_{ELF}^{x64}).

² DEEPT_{ref}’s reference model has no knowledge of ICC-built binaries, thus in the testing dataset for the accuracy of DEEPT_{ref}, we exclude the ICC-built binaries from the ground truths.

stack details, such as pointer dereference, which cannot be resolved statically. Following the DWARF-based memory block extraction, we utilize the iVTR analysis in Section 3.3.1 to obtain the ground truth *BRel* instructions. The labeled instructions extracted from SP_{train}^{x86} are then employed to train the DISA deep model for T_3 , while the ground truth *BRel* instructions from SP_{test}^{x86} are utilized for evaluations in Section 5.5.

5.2 Baselines

To answer RQ1, RQ2, and RQ4, we use the learning-based approaches, XDA [46], biRNN [53], and DEEPT_{ref} [69] as the baselines. We train the biRNN deep models and finetune the XDA deep models using our datasets (more details in Appendix A). We have yet to obtain DEEPT_{ref}’s implementation to train the deep model but can only access the released DEEPT_{ref} model through its APIs. We call such a deep model the reference model DEEPT_{ref} in Table 2. Table 2 denotes the deep models with the *approach name* followed by the *training dataset*. Specifically, XDA-SN, biRNN-SN, and DISA-SN are the deep models trained/finetuned by the randomly selected 90% of dataset SN. The rest 10% of SN, i.e., SN_{test}^2 , is the testing dataset. The models of different tasks (T_1 and T_2) are trained with different ground truths; thus, for example, DISA-SN has two deep models, one for task T_1 and the other for task T_2 . These models are the most general models we can obtain to compare with DEEPT_{ref}’s reference model on accuracy and generalizability. Moreover, we train more deep models with the dataset SN_{ELF}^{x64} , called *x64ELF-centric* models, to further investigate the generalizability, despite their incomparability with DEEPT_{ref}. We also train optimization-level-specific deep models, e.g., DISA- SN_{ELF}^{x64} -00, standing for the DISA model trained with the 00-binaries of SN_{ELF}^{x64} . Besides the deep models, We also use the popular reverse-engineering frameworks IDA Pro 7.6, Ghidra 10.3, and Binary Ninja 4.0 under their default settings as baselines. To make fair comparisons with these frameworks, we input the stripped binaries to these frameworks in our testing. The metrics of RQ1 and RQ2 are the *precision* (P), *recall* (R), and F1-score.

To answer RQ3, our baselines are BPA and BPA_{DWARF}. Similar to BPA_{DISA}, the BPA_{DWARF} is another modified version of BPA, which utilizes DWARF-based memory blocks instead of BPA’s heuristics-based memory blocks. The memory blocks based on DWARF use debugging information to create the most precise memory blocks. Therefore, for analysis methods like BPA that rely on memory block-based aliasing analysis, these nearly perfect memory blocks are expected to produce the best possible indirect call target result. Thus, BPA_{DWARF} represents the most achievable reference version of BPA. To address RQ3’s first question, we assess the effectiveness of memory blocks generated by DISA compared to those from BPA,

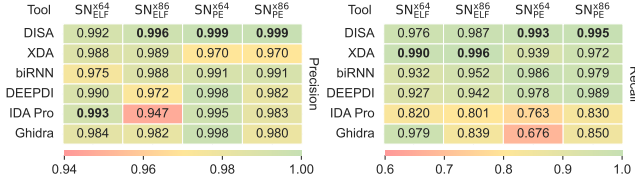


Figure 6: T_1 Accuracy Heatmaps on Different Platforms and ISA Variants

using DWARF-based memory blocks as the ground truth reference. To define the *precision*, *recall*, and F1-score in this scenario, a true positive (TP) indicates a correctly generated memory block that aligns with a block found in the reference ground truth. A false positive (FP) refers to a generated memory block that does not appear in the ground truth, while a false negative (FN) signifies a block present in the ground truth but absent from the memory block generation of DISA or BPA. To evaluate the second question of RQ3, we adopt the classic metric, AICT (Average Indirect Call Targets), to assess accuracy. We also measure the recall to assess soundness, where a higher recall value indicates a smaller number of missed indirect call target predictions, which results in a more comprehensive CFG construction. We leverage a Pin tool to gather runtime profile data for the SP_{test}^{x86} benchmarks under the ref workloads for recall checks. Once we obtain the call-traces, following BPA, we calculate the average recall for all indirect calls using

$$Rc = \frac{1}{n} \sum_{i=1}^n Rc_i \quad \text{where} \quad Rc_i = \frac{TP_i}{TP_i + FN_i}$$

Measuring precision is feasible. Considering that the precision can be estimated from a high recall and the AICT, we ignore this metric for simplicity.

5.3 Accuracy (RQ1)

We evaluate the accuracy of different learning-based approaches on four subsets of the testing dataset SN_{test}. We report the precision and recall on T_1 in Fig. 6. Because DEEPDI's model training did not use the ICC-built binaries, we ignore the ground truths of the ICC-built binaries to decide DEEPDI's accuracy. Meanwhile, we also present IDA Pro and Ghidra's results on the complete four subsets of SN. In predicting the function entries, DISA has the best accuracy on SN_{PE}. On SN_{ELF}, XDA has the best F1-score while DISA has better precision than XDA. The traditional frameworks allow more false negatives but are competitive in precision compared with the learning-based approaches. On the PE binaries, the main reason is that we use the symbol table to collect the function boundary ground truth. The traditional frameworks, e.g., IDA Pro, do not focus on resolving specific library function entries.

5.4 Generalizability (RQ2)

This section evaluates DISA's robustness. Specifically, we compare the deep models' generalizability in different scenarios, including on unseen real-world binaries and obfuscated binaries. We also discuss the cross-optimization-level generalizability of different deep models.

5.4.1 Generalizability on Unseen Real-World Binaries. We evaluate the robustness of different approaches on the real-world binaries

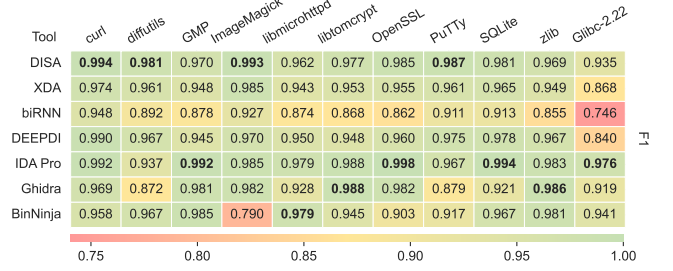


Figure 7: T_1 Generalizability Heatmap in Predicting Unseen Real-World x64-ELF Binaries

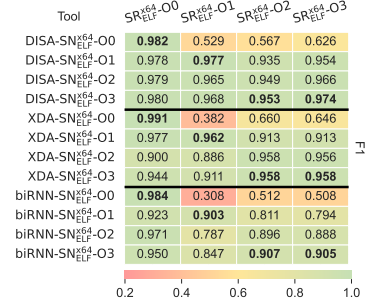


Figure 8: T_1 Cross-Optimization-Level Generalizability Heatmap on Real-World x64-ELF Binaries

in SR_{ELF}^{x64}, as presented in Fig 7. Generally, in task T_1 , DISA and IDA Pro outperform other approaches. DISA shows a 1.8% F1-score improvement over other deep-learning approaches in identifying function entries. Specifically, the deep models' effectiveness on Glibc is not as good as on other programs due to its more complex function entries and the inline assembly code. In this case, IDA Pro outperforms others. In task T_2 , the deep models all report F1>99% (Fig. 16 in Appendix B). XDA outperforms other deep models in identifying instructions of real-world binaries. We infer that XDA's code-byte classification excels in more balanced classification. In contrast, with the high-level features, our superset-instruction classification could deal better with more imbalanced data for function entry-point identification.

Unseen compiler optimization flags can introduce new instruction patterns and challenge the disassembly effectiveness. To this end, we first investigate the optimization-level-specific deep models' capability of cross-optimization-level predictions on real-world binaries. From Fig. 8, we know that for several optimization-level-specific models even not on O0, making predictions on O0-binaries is easier than on O1-O3. The O0 models are extremely weak in predicting function entries of the binary on other optimization levels. Then, we conduct another cross-optimization-level evaluation over the binaries built with the optimization flag combinations discovered by BinTuner. For a specific program, BinTuner can find the extremely complex optimization option for building the binary in maximum *normalized compression distance* (NCD) with a baseline compilation configuration. In Fig. 9, we use four real-world programs, i.e., httpd, SQLite, bzip2, and diffutils. We use the O0 binary of these programs as BinTuner's baseline for maximizing NCD. The optimization flag combinations discovered by BinTuner are on O1-O3. Thus, for the cross-optimization-level evaluation, we use

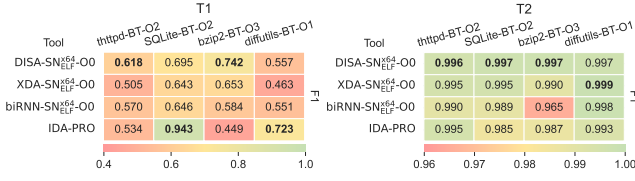


Figure 9: Generalizability Heatmap on Real-World Binaries on BinTuner Discovered Complex Optimization Options

the O0 deep models to decide the function entries and instructions. From Fig. 9, we observe that BinTuner poses a significant challenge to the function entry-point identification but a minimal difficulty to the instruction disassembly. DISA outperforms other deep models in most of these cases.

5.4.2 Generalizability on Obfuscated Binaries. We compare the generalizability of the learning-based approaches in deciding the function entries and instructions of the obfuscated binaries of SO. Apart from the best deep models of different approaches, we will also investigate whether the x64ELF-centric models could reach better performance. Besides, we enable the compiler optimizations to investigate the impact of different optimizations on the obfuscation.

Fig. 10 presents the function entry-point identification results on obfuscated binaries. The top half of Fig. 10 presents the most general effect of different approaches. The bottom half presents the results of the x64ELF-centric models. Generally, IDA Pro and Ghidra have high precision while the deep models achieve better recall. On ollvm-obfuscated binaries (SO_{ELF}^{OLL}), IDA Pro, DEEPDI, and DISA’s x64ELF-centric model are the leading approaches. On both the general and x64ELF-centric models, DISA reports higher precision than XDA, while XDA enforces higher recalls.

Desync-cc and tigress have more intensive effects on disrupting function entries than ollvm. On SO_{ELF}^{DSY} , DISA’s general model and x64ELF-centric model respectively outperform other approaches by 9.1% and 5.7% in F1-score. Therefore, DISA has a significant advantage in detecting function entries of the binary obfuscated with the desynchronization technique. To investigate the reason for DISA’s advantage on SO_{ELF}^{DSY} , we conduct case studies on several SPEC2017 binaries. On several functions starting with mov, lea, or logical and instruction, XDA and DEEPDI have false negatives. DEEPDI also ignores several function entries when the starting push instruction follows the desync-cc-inserted junk bytes. The false positives of XDA and DEEPDI are observed on several desync-cc-inserted push instructions and junk bytes. Generally, DEEPDI’s GRU-model based function entry-point recovery only uses short instruction contexts and thus is less capable than DISA in T_1 . DISA’s instruction-level function entry knowledge benefits the differentiation of desync-cc-inserted junk bytes compared to the byte-level knowledge used by XDA. Regarding IDA Pro and Ghidra, they raise decoding errors on a considerable portion of instructions, thus failing to resolve function entries due to the missing instructions.

On tigress-obfuscated binaries (SO_{PE}^{TGR}), the model DISA-SN outperforms other approaches by 13.2% in F1-score, while IDA Pro has the best precision. In general, on source-level obfuscators like ollvm and tigress, the deep models do not have a significant advantage over the traditional frameworks, e.g., IDA Pro. In the function entry-point identification, we did not observe the interference from

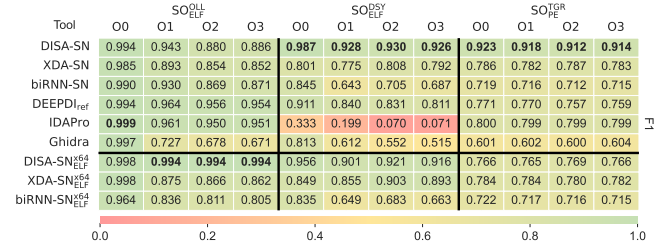


Figure 10: T_1 Generalizability Heatmap in Predicting Obfuscated Binaries at Different Optimization Levels

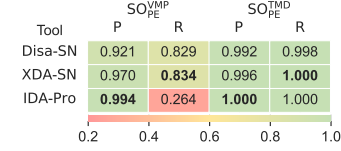


Figure 11: T_2 Generalizability Heatmap in Predicting VMProtect and Themida-obfuscated PE binaries

compiler optimizations to the obfuscation, which was assumed by [46], and the compiler optimizations are disabled by [46, 69]. In many cases, the deep models have lower effectiveness on O1-O3 binaries than on O0 binaries, indicating that obfuscation combined with optimizations causes more intensive disruption to the pattern of function prologues.

Identifying instructions in obfuscated binaries is more straightforward than identifying function entries for the deep models (Fig. 17 in Appendix B). In task T_2 , IDA Pro is most effective on ollvm-obfuscated binaries. DEEPDI_{ref} and XDA-SN have the best instruction-level F1-score respectively on desync-cc-obfuscated and tigress-obfuscated binaries. When using the x64ELF-centric model, DISA-SN^{x64} outperforms others on desync-cc-obfuscated binaries. In addition, we performed testing on the VMProtect and Themida-obfuscated binaries, i.e., SO_{PE}^{VMP} and SO_{PE}^{TMD} . As Fig. 11 presented, the deep models outperform IDA Pro in F1-score when predicting the instructions in the .vmp2 section of VMProtect-obfuscated binaries. Disassembling the .text section of Themida-protected binary is easier for the tools to reach F1≥99%, while IDA Pro has the best F1-score.

In summary, DISA is more robust than other approaches to identify function entries, improving other deep-learning approaches by 1.8% on unseen real-world binaries, 9.1% on desync-cc-obfuscated binaries, and 13.2% on tigress-obfuscated binaries. Besides, DISA’s x64ELF-centric model outperforms other approaches in identifying instructions of desync-cc-obfuscated binaries.

5.5 Memory Block Boundary Determination and Security Effect (RQ3)

We first compare DISA’s memory block prediction effectiveness with BPA’s original heuristic-based memory block boundary identification. Then, we evaluate BPA_{DISA}’s accuracy in identifying indirect targets by comparing it with BPA and BPA_{DWARF}. Furthermore, after a case study on indirect call resolution, we conduct an ablation study to demonstrate each component’s contribution to indirect call resolution.

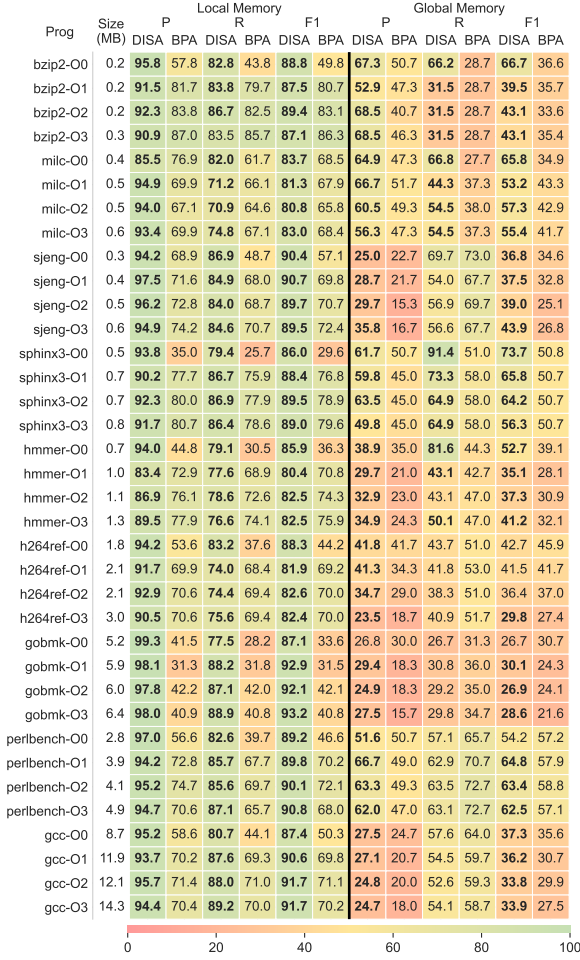


Figure 12: Effectiveness Heatmap of Disa on Deciding Memory Block Boundaries Compared with BPA (in Percentage)

5.5.1 Effectiveness On Memory Block Boundary Generations. We compared the memory block generation of Disa with that of BPA’s heuristic-based approach in terms of precision, recall, and F1-score defined in Section 5.2. This comparison allows us to assess the effectiveness of Disa in minimizing false positive predictions and enhancing precision, which is vital for downstream applications such as indirect target identification.

Compared to BPA, Disa demonstrates an average enhancement of 18.5% in precision, 11.6% in recall, and 16.1% in F1-score when generating memory blocks. The prediction of memory blocks is further divided into local and global types. In local memory block partitioning, Disa achieves an impressive 27% and 24% improvement in precision and F1-score respectively compared with BPA, as presented in Fig. 12. The local memory block prediction is uniformly good across increased binary complexity as well as different optimization levels. Disa generally offers better local memory block boundaries than global memory.

Both Disa and BPA encounter significant challenges in accurately predicting global memory accesses. Our manual inspections on SP^{x86}_{test} binaries reveal that global memory block start addresses are seldom loaded directly into registers; rather, they are typically

Table 3: AICT and Recall Comparison between BPA_{Disa} , BPA_{DWARF} , and BPA on SP^{x86}_{test} (for GCC 9.2.0)

Program	#Callsite	AICT			Recall		
		BPA_{DWARF}	BPA	BPA_{Disa}	BPA_{DWARF}	BPA	BPA_{Disa}
hmmcr-O0	9	2.8	2.9	2.8	100	100	100
hmmcr-O1	11	4.3	4.3	4.3	100	100	100
hmmcr-O2	10	2.7	2.8	2.8	100	100	100
hmmcr-O3	9	1.0	1.0	1.0	100	100	100
h264ref-O0	369	4.2	5.7	4.3	100	100	100
h264ref-O1	353	4.1	5.2	5.2	99.7	99.7	99.7
h264ref-O2	352	26.4	26.7	26.9	100	100	100
h264ref-O3	355	18.0	18.5	18.6	99.7	99.7	100
gobmk-O0	44	846.9	884.6	846.9	100	100	100
gobmk-O1	44	1334.7	1336.3	1336.3	100	100	100
gobmk-O2	44	1337.7	1337.7	1337.7	100	100	100
gobmk-O3	44	1416.2	1416.2	1416.2	100	100	100
perlbench-O0	139	388.9	400.3	387.6	100	100	99.1
perlbench-O1	139	370.1	379.7	379.7	100	100	100
perlbench-O2	110	371.2	377.6	373.9	100	100	100
perlbench-O3	237	453.4	453.4	456.4	100	100	100
gcc-O0	459	89.4	540.8	447.1	95.4	99.3	95.3
gcc-O1	473	336.1	496.9	338.1	96.0	99.5	95.8
gcc-O2	450	414.7	440.9	431.1	96.6	99.5	96.2
gcc-O3	727	441.6	526.7	454.1	97.8	99.6	96.2

accessed indirectly through complex pointer arithmetic. For example, in the dataset SP^{x86}_{test} , 50% of global memory blocks are accessed this way, with none of their starting addresses being explicitly loaded in the user code. Accurately predicting them continues to pose challenges for both Disa and BPA. Furthermore, some compiler-allocated global memory blocks remain entirely unaccessed in user code, further complicating prediction accuracy. In addition, Disa’s intra-procedural value tracking fails to account for global accesses that are passed through function arguments. Additionally, repetitive patterns such as loops can lead to false positives, as mentioned in Section 3.3.

To overcome the global memory block prediction limitations, in Disa, we have integrated the strengths of T_3 ’s machine learning-based predictions with BPA’s traditional static analysis. This hybrid approach has enhanced precision by leveraging T_3 ’s pattern identification alongside a modest increase in recall from BPA’s conservative analysis, as illustrated in Fig. 12. On average, Disa achieves a 10.1% improvement in precision and an 8.1% improvement in F1-score for global memory blocks compared with BPA. Notably, Disa has enhanced global memory block precision for most programs in SP^{x86}_{test} . Disa has surpassed BPA in F1-score across all other binaries in SP^{x86}_{test} except for h264ref. The primary reason for the performance dip in h264ref is also the complex pointer arithmetic involved in global block accessing.

Additionally, our evaluation demonstrates that Disa improves the metrics at each optimization level. As program complexity increases, Disa exhibits more conservative memory block partitioning and outperforms BPA at higher optimization levels, making it a more suitable tool for analyzing larger, real-world binaries.

5.5.2 Indirect Call Target Comparison. We evaluate the ability to resolve indirect call targets using BPA’s block-boundary-based points-to analysis. The evaluation compares AICT values produced by original BPA, BPA_{Disa} , and BPA_{DWARF} , as presented in Table 3. For conciseness, we omit the results for bzip2, milc, sjeng, and sphinx3, as all three schemes achieve identical AICT as well as 100% recall.

Table 3 supports Disa’s effectiveness in improving the indirect call targets prediction and substantiates our hypothesis about BPA_{DWARF} ’s ultimate performance in Section 5.2. Compared to

BPA_{DWARF}. BPA shows deficiency in 15 out of 36 benchmarks in terms of AICT, while BPA_{DISA} matches BPA_{DWARF}'s performance in 9 instances, indicating its superiority over BPA. DISA's advantage on memory block generation in Fig. 12 leads to noticeable AICT decreases for 00 binaries and the more complex binaries in Table 3. As program complexity increases, BPA's heuristic-based memory-block generation becomes limited, while BPA_{DISA} demonstrates better results, e.g., for benchmarks gobmk-00, perlbench-00, and gcc. In profiling-based evaluation, we observed good recalls of BPA_{DISA} and BPA in alignment with BPA_{DWARF} and a better precision of BPA_{DISA} for larger binaries. In addition, for h264ref-03, we observe increased recall rates, indicating more coverage of the indirect call targets with increased AICT. Furthermore, We noted a slight decrease in AICT for perlbench-00 compared with BPA_{DWARF}, attributed to missing targets and reduced recall rates. Additionally, perlbench-03 and h264ref-02 had an indirect call prediction that neither BPA nor BPA_{DWARF} reported. This observation indicates that DISA's higher recall in this case in Fig. 12 cannot avoid a false negative prediction on specific memory block boundary to introduce certain false indirect targets. In addition, we identify a discrepancy between our reevaluation of BPA and the original results presented in [32]. Upon closer investigation, we confirm that an implementation issue mishandles finer-grained and coarse-grained memory blocks and causes this deviation.

5.5.3 Case Study. The accurate resolution of indirect function calls remains a significant challenge for commercial tools. In contrast, BPA_{DISA} delivers more precise CFGs than these tools. This case study examines the resolution of indirect calls within the bzip2 benchmark, using the source code for clarity. Notably, the same phenomenon can also be observed in the binary version of the code.

In bzip2, indirect calls specifically occur within two memory management functions: default_bzalloc and default_bzfree. Listing 1 is a code snippet from bzip2 that defines a memory allocation structure and the corresponding default allocation functions. The allocation and deallocation functions are set as defaults within the BZ2_bzCompressInit function, as illustrated in Listing 2. Additionally, indirect calls made via BZALLOC and BZFREE reference the functions default_bzalloc and default_bzfree, respectively. These indirect calls are utilized in function BZ2_decompress, which is detailed in Listing 3. Specifically, function BZ2_decompress invokes default_bzalloc through BZALLOC. Analysis with IDA and Ghidra shows that both tools fail to resolve the indirect calls to the function default_bzalloc. In function BZ2_decompress, they only identify direct calls to fprintf, fwrite, BZ2_indexIntoF, makeMaps_d, BZ2_hbCreateDecodeTables, and BZ2_bz_AssertH_fail.

In addition, our PIN tool-based detection framework effectively captures indirect calls to the default_bzalloc function, confirming its reachability. This showcases BPA_{DISA}'s ability to create comprehensive CFGs. Our ability to resolve indirect call targets precisely is enabled by a practical block-based points-to analysis, where the precision of memory blocks is critical. DISA T_3 model helps us achieve this precision, resulting in clearer points-to sets and better resolution of indirect call targets. While this study focuses on a small binary, we confirm that similar issues exist in larger binaries, further validating our method's superiority.

Listing 1: Memory allocation structure and associated calls

```
typedef struct {
    void *(*bzalloc)(void *, int, int);
    void (*bzfree)(void *, void *);
    void *opaque;
} bz_stream;
static void* default_bzalloc(void* opaque, int items, int size) {
    return malloc(items * size);
}
static void default_bzfree(void* opaque, void* addr) {
    if (addr != NULL) free(addr);
}
```

Listing 2: Indirect initialization of calls

```
int BZ_API(BZ2_bzCompressInit)(bz_stream* strm,_,_,_) {
    if (strm->bzalloc == NULL) strm->bzalloc = default_bzalloc;
    if (strm->bzfree == NULL) strm->bzfree = default_bzfree;
}
...
#define BZALLOC(nnn) (strm->bzalloc)(strm->opaque, (nnn), 1)
#define BZFREE(ppp) (strm->bzfree)(strm->opaque, (ppp))
```

Listing 3: Indirect Calls in BZ2_decompress

```
if (s->smallDecompress) {
    s->l116 = BZALLOC(s->blockSize100k * num * sizeof(_));
    s->l14 = BZALLOC(((1 + s->blockSize100k * num) >> 1) * sizeof(_));
    if (s->l116 == NULL || s->l14 == NULL) RETURN(BZ_MEM_ERROR);
} else {
    s->tt = BZALLOC(s->blockSize100k * num * sizeof(_));
    if (s->tt == NULL) RETURN(BZ_MEM_ERROR);
}
```

Table 4: AICT and Recall Comparison between BPA_{DISA}, BPA_{DISA}^{T1}, BPA_{DISA}^{T2}, and BPA_{DISA}^{T12} on SPx86 test (for GCC 9.2.0)

Program	AICT				Recall			
	BPA _{DISA}	BPA _{DISA} ^{T1}	BPA _{DISA} ^{T2}	BPA _{DISA} ^{T12}	BPA _{DISA}	BPA _{DISA} ^{T1}	BPA _{DISA} ^{T2}	BPA _{DISA} ^{T12}
milc-00	2.0	2.0	1.0	1.0	100.0	100.0	50.0	50.0
milc-01	2.0	2.0	2.0	2.0	100.0	100.0	100.0	100.0
milc-02	2.0	2.0	2.0	2.0	100.0	100.0	100.0	100.0
milc-03	1.0	0.8	1.0	0.8	100.0	75.0	100.0	75.0
sjeng-00	7.0	7.0	7.0	7.0	100.0	100.0	100.0	100.0
sjeng-01	7.0	6.0	7.0	6.0	100.0	100.0	100.0	100.0
sjeng-02	7.0	7.0	7.0	7.0	100.0	100.0	100.0	100.0
sjeng-03	7.0	7.0	7.0	7.0	100.0	100.0	100.0	100.0
h264ref-00	4.3	4.3	4.3	4.3	100.0	100.0	100.0	100.0
h264ref-01	5.2	5.2	5.2	5.2	99.7	99.7	99.7	99.7
h264ref-02	26.9	26.9	26.9	26.9	100.0	100.0	100.0	100.0
h264ref-03	18.6	17.9	18.6	17.9	100.0	100.0	100.0	100.0
gobmk-00	846.9	846.9	846.9	846.9	100.0	100.0	100.0	100.0
gobmk-01	1336.3	1333.3	1336.3	1333.3	100.0	99.7	100.0	99.7
gobmk-02	1337.7	1330.3	1337.7	1330.3	100.0	100.0	100.0	100.0
gobmk-03	1416.2	1408.3	1416.2	1408.3	100.0	100.0	100.0	100.0
perlbench-00	387.6	387.8	387.8	387.8	99.1	99.1	99.1	99.1
perlbench-01	379.7	371.3	380.0	371.3	100.0	100.0	100.0	100.0
perlbench-02	373.9	372.9	374.0	372.9	100.0	100.0	100.0	100.0
perlbench-03	456.4	463.4	465.4	463.4	100.0	100.0	100.0	100.0

5.5.4 Ablation Study. To evaluate the contribution of each component of DISA, we began by integrating BPA_{DISA} with T_1 , resulting in BPA_{DISA}^{T1}. Similarly, we replaced BPA_{DISA} instruction boundary with the boundary of T_2 , yielding BPA_{DISA}^{T2}. Finally, we combined all three tasks of DISA with BPA_{DISA}, resulting in BPA_{DISA}^{T12}. The evaluation results are presented in Table 4. As shown, incorporating the three DISA-supported tasks into BPA enhances the effectiveness of control flow graph recovery than only T_3 -supported DISA, i.e.,

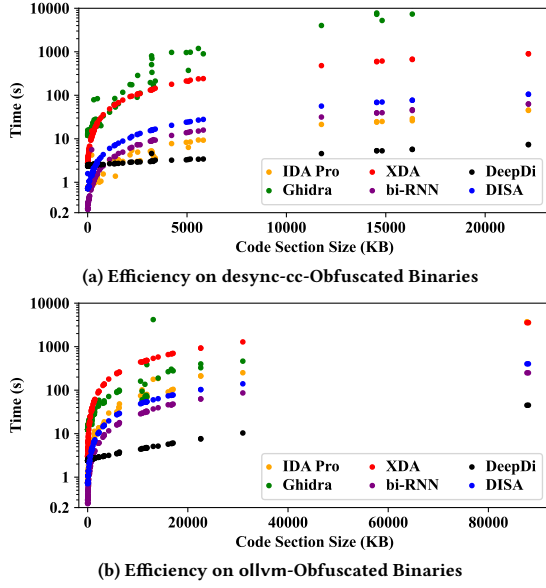


Figure 13: Task T_2 Efficiency on Obfuscated Binaries

original BPA_{DISA}, especially for larger and more highly optimized binaries like gobmk and perlbench. In addition, it maintains a high recall rate for the majority, indicating its overall capability of covering the attack surface. For conciseness, we omit the results for bzip2, hmmmer, and sphinx3, as all four schemes achieve identical AICT as well as 100% recall. We excluded the GCC benchmark from the ablation study due to its significantly higher evaluation time and memory requirements.

5.6 Efficiency (RQ4)

We evaluate the efficiency of different approaches to identify instructions of the SO_{ELF}^{DSY} and SO_{ELF}^{OLL} binaries. The prediction procedures of the learning-based approaches are on the NVIDIA A10 GPU, while DISA’s multi-thread superset disassembly procedure is on the CPU. The metric is the time cost from the binary input to all its code bytes or superset instructions getting classified completely. According to the specific results in Fig. 13, the costs of learning-based approaches are stably correlated with the code section size. Among the learning-based approaches, DEEPDI is the most efficient due to the moderate model size and the GPU-accelerated superset disassembly. DISA’s multi-thread superset disassembly takes 3.55 seconds on average on each binary, which tends to be more costly than DEEPDI. DISA is more costly than biRNN since biRNN has simpler models (Table 6 in Appendix B). XDA is more costly than DISA in both prediction and model generation. The costs of the traditional frameworks are irregular on different obfuscators. IDA Pro is more efficient on desync-cc than on llvm because on the desync-cc-obfuscated binaries, it fails to reach several portions of the code section. Ghidra has extremely high costs on desync-cc-obfuscated binaries. Ghidra raises warnings about function body repairing on desync-cc-obfuscated binaries, indicating its inefficacy in handling desynchronization technique. In summary, DISA is more efficient

than XDA and Ghidra and is competitive with IDA Pro, making it a scalable approach for real-world usage.

6 Discussion

Even though DISA’s major goal is to enhance BPA with improved memory blocks, we still compare our BPA_{DWARF} and BPA_{DISA} with the AICT metrics reported by the state-of-the-art indirect call prediction methods, CALLEE[72] and AttnCall[58]. BPA_{DWARF} outperforms the others in 5 out of 9 benchmarks, i.e., milc, sphinx3, hmmmer, h264ref, and gcc. Notably, for the largest benchmark, gcc, BPA_{DWARF} demonstrates a significant 67.4% decrease in AICT compared with the state-of-the-art. BPA_{DISA} approaches BPA_{DWARF} in 4 out of those 5 benchmarks, showing potential in surpassing the state-of-the-art methods.

Besides, DISA can be applied to other security applications that rely on memory blocks or similar concepts. One possibility is to enhance binary fuzzing through hardware-assisted memory sanitizer [19]. A critical part of the system is an object recovery scheme that progressively recovers object boundaries, resembling our memory blocks. The progressive object recovery relies on access patterns-based heuristics, which we propose to replace with our more precise memory blocks to enhance the binary fuzzing process. It would also be an interesting future work to compare DISA’s T_1 and T_2 capability with the LLM-based approach [50].

7 Conclusion

DISA is a new deep-learning-based disassembly approach based on the multi-head attention mechanism to classify superset instructions and achieve more precise boundary identifications. DISA disassembly framework uniquely supports predicting memory block boundaries. We have integrated it with existing block memory model-based value set analysis to resolve the indirect call targets for the accurate binary-level CFG construction. We have demonstrated that DISA improves instruction and function entry-point identification, even for the binaries built with different obfuscators, and produces more accurate CFGs by establishing more precise memory block boundaries.

References

- [1] 2010. DWARF Debugging Information Format Version 4. <https://dwarfstd.org/doc/DWARF4.pdf>.
- [2] 2013. Obfuscator-LLVM. <http://o-llvm.org>.
- [3] 2014. C tutorial for Capstone. https://www.capstone-engine.org/lang_c.html
- [4] 2021. desync-cc – Automatic Disassembly Desynchronization Obfuscator. <https://github.com/UlfKargen/desync-cc>
- [5] 2024. Dia2dump Sample. <https://learn.microsoft.com/en-us/visualstudio/debugger/debug-interface-access/dia2dump-sample?view=vs-2022>.
- [6] Dennis Andriess, Xi Chen, Victor van der Veen, Asia Slowinska, and Herbert Bos. 2016. An In-Depth Analysis of Disassembly on Full-Scale x86/x64 Binaries. In *25th USENIX Security Symposium*. USENIX Association, 583–600.
- [7] Dennis Andriess, Asia Slowinska, and Herbert Bos. 2017. Compiler-Agnostic Function Detection in Binaries. In *EuroS&P’17*. IEEE, 177–189.
- [8] Gogul Balakrishnan and Thomas W. Reps. 2004. Analyzing Memory Accesses in x86 Executables. In *CC’04 (LNCS, Vol. 2985)*. Springer, 5–23.
- [9] Tiffany Bao, Jonathan Burket, Maverick Woo, Rafael Turner, and David Brumley. 2014. BYTEWEIGHT: Learning to Recognize Functions in Binary Code. In *23rd USENIX Security Symposium*. USENIX Association, 845–860.
- [10] Sébastien Bardin, Robin David, and Jean-Yves Marion. 2017. Backward-Bounded DSE: Targeting Infeasibility Questions on Obfuscated Codes. In *SP’17*. IEEE, 633–651.
- [11] Erick Bauman, Zhiqiang Lin, and Kevin W. Hamlen. 2018. Superset Disassembly: Statically Rewriting x86 Binaries Without Heuristics. In *NDSS’18*. The Internet Society.

- [12] M. Ammar Ben Khadra, Dominik Stoffel, and Wolfgang Kunz. 2016. Speculative disassembly of binary code. In *CASES'16*. ACM, 16:1–16:10.
- [13] Eli Bendersky. 2011. pyelftools. <https://github.com/eliben/pyelftools>.
- [14] Hadjer Benkraouda, Nirav Diwan, and Gang Wang. 2025. You Can't Judge a Binary by Its Header: Data-Code Separation for Non-Standard ARM Binaries Using Pseudo Labels. In *SP '25*. IEEE, 3727–3745.
- [15] Andrew R. Bernat and Barton P. Miller. 2011. Anywhere, any-time binary instrumentation. In *PASTE'11*. ACM, 9–16.
- [16] Guillaume Bonfante, José M. Fernandez, Jean-Yves Marion, Benjamin Rouxel, Fabrice Sabatier, and Aurélien Thierry. 2015. CoDisasm: Medium Scale Concat Disassembly of Self-Modifying Binaries with Overlapping Instructions. In *CCS'15*. ACM, 745–756.
- [17] David Brumley, Ivan Jager, Thanassis Avgerinos, and Edward J. Schwartz. 2011. BAP: A Binary Analysis Platform. In *CAV'11 (LNCS, Vol. 6806)*. Springer, 463–469.
- [18] Juan Caballero and Zhiqiang Lin. 2016. Type Inference on Executables. *ACM Comput. Surv.* 48, 4 (2016), 65:1–65:35.
- [19] Xingman Chen, Yinghao Shi, Zheyu Jiang, Yuan Li, Ruoyu Wang, Haixin Duan, Haoyu Wang, and Chao Zhang. 2023. MTSan: A Feasible and Practical Memory Sanitizer for Fuzzing COTS Binaries. In *32nd USENIX Security Symposium*. USENIX Association, 841–858.
- [20] Christian Collberg. [n. d.]. The Tigress C Obfuscator. <https://tigress.wtf/index.html>.
- [21] Cryptic Apps. [n. d.]. Hopper: The macOS and Linux Disassembler. <https://www.hopperapp.com>.
- [22] Alessandro Di Federico, Mathias Payer, and Giovanni Agosta. 2017. rev.ng: a unified binary analysis framework to recover CFGs and function boundaries. In *CC '17*. ACM, 131–141.
- [23] Antonio Flores-Montoya and Eric M. Schulte. 2020. Datalog Disassembly. In *29th USENIX Security Symposium*. USENIX Association, 1075–1092.
- [24] GNU. 2023. GNU Binutils 2.40. <https://www.gnu.org/software/binutils>.
- [25] M.R. Guthaus, J.S. Ringenberg, D. Ernst, T.M. Austin, T. Mudge, and R.B. Brown. 2001. MiBench: A free, commercially representative embedded benchmark suite. In *Proceedings of the Fourth Annual IEEE International Workshop on Workload Characterization. WWC-4 (Cat. No. 01EX538)*. 3–14.
- [26] Jingxuan He, Pesho Ivanov, Petar Tsankov, Veselin Raychev, and Martin T. Vechev. 2018. Debin: Predicting Debug Information in Stripped Binaries. In *CCS'18*. ACM, 1667–1680.
- [27] Hex-Rays. 2021. IDA Pro. <https://hex-rays.com/IDA-pro>.
- [28] Minkyu Jung, Soomin Kim, HyungSeok Han, Jaeseung Choi, and Sang Kil Cha. 2019. B2R2: Building an Efficient Front-End for Binary Analysis. In *The Workshop on Binary Analysis Research*.
- [29] Pascal Junod, Julien Rinaldini, Johan Wehrli, and Julie Michielin. 2015. Obfuscator-LLVM – Software Protection for the Masses. In *IEEE/ACM 1st International Workshop on Software Protection, SPRO'15*. IEEE, 3–9.
- [30] Ulf Kargen, Ivar Härnqvist, Johannes Wilson, Gustav Eriksson, Evelina Holmgren, and Nahid Shahmehri. 2022. desync-cc: An Automatic Disassembly-Desynchronization Obfuscator. In *SANER'22*. IEEE, 464–468.
- [31] Jacob Devlin Ming-Wei Chang Kenton and Lee Kristina Toutanova. 2019. Bert: Pre-training of deep bidirectional transformers for language understanding. In *Proceedings of naacl-HLT, Vol. 1*. 2.
- [32] Sun Hyoung Kim, Cong Sun, Dongrui Zeng, and Gang Tan. 2021. Refining Indirect Call Targets at the Binary Level. In *NDSS'21*. The Internet Society.
- [33] Sun Hyoung Kim, Dongrui Zeng, Cong Sun, and Gang Tan. 2022. BinPointer: towards precise, sound, and scalable binary-level pointer analysis. In *CC '22*. ACM, 169–180.
- [34] Hyungjoon Koo, Soyeon Park, and Taesoo Kim. 2021. A Look Back on a Function Identification Problem. In *ACSAC '21*. ACM, 158–168.
- [35] Christopher Krügel, William K. Robertson, Fredrik Valeur, and Giovanni Vigna. 2004. Static Disassembly of Obfuscated Binaries. In *13th USENIX Security Symposium*. USENIX Association, 255–270.
- [36] Xuezixiang Li, Yu Qu, and Heng Yin. 2021. PalmTree: Learning an Assembly Language Model for Instruction Embedding. In *CCS '21*. ACM, 3236–3251.
- [37] Tsung-Yi Lin, Priya Goyal, Ross B. Girshick, Kaiming He, and Piotr Dollár. 2017. Focal Loss for Dense Object Detection. In *ICCV'17*. IEEE, 2999–3007.
- [38] Yan Lin and Debin Gao. 2021. When Function Signature Recovery Meets Compiler Optimization. In *SP'21*. IEEE, 36–52.
- [39] Alwin Maier, Hugo Gascon, Christian Wressnegger, and Konrad Rieck. 2019. TypeMiner: Recovering Types in Binary Programs Using Machine Learning. In *DIMVA '19 (LNCS, Vol. 11543)*. Springer, 288–308.
- [40] Kenneth A. Miller, Yonghwi Kwon, Yi Sun, Zhuo Zhang, Xiangyu Zhang, and Zhiqiang Lin. 2019. Probabilistic disassembly. In *ICSE'19*. IEEE / ACM, 1187–1198.
- [41] Paul Muntean, Matthias Fischer, Gang Tan, Zhiqiang Lin, Jens Grossklags, and Claudia Eckert. 2018. rCFI: Type-Assisted Control Flow Integrity for x86-64 Binaries. In *RAID'18 (LNCS, Vol. 11050)*. Springer, 423–444.
- [42] NSA. 2019. Ghidra Software Reverse Engineering Framework. <https://github.com/NationalSecurityAgency/ghidra>.
- [43] Chengbin Pang, Ruotong Yu, Yaohui Chen, Eric Koskinen, Georgios Portokalidis, Bing Mao, and Jun Xu. 2021. SoK: All You Ever Wanted to Know About x86/x64 Binary Disassembly But Were Afraid to Ask. In *SP'21*. IEEE, 833–851.
- [44] Adam Paszke, Sam Gross, Francisco Massa, Adam Lerer, James Bradbury, Gregory Chanan, Trevor Killeen, Zeming Lin, Natalia Gimelshein, Luca Antiga, Alban Desmaison, Andreas Köpf, Edward Z. Yang, Zachary DeVito, Martin Raison, Alykhan Tejani, Sasank Chilamkurthy, Benoit Steiner, Lu Fang, Junjie Bai, and Soumith Chintala. 2019. PyTorch: An Imperative Style, High-Performance Deep Learning Library. In *NeurIPS '19*. 8024–8035.
- [45] Kexin Pei, Jonas Guan, Matthew Broughton, Zhongtian Chen, Songchen Yao, David Williams-King, Vikas Ummadisetti, Junfeng Yang, Baishakhi Ray, and Suman Jana. 2021. StateFormer: fine-grained type recovery from binaries using generative state modeling. In *ESEC/FSE '21*. ACM, 690–702.
- [46] Kexin Pei, Jonas Guan, David Williams-King, Junfeng Yang, and Suman Jana. 2021. XDA: Accurate, Robust Disassembly with Transfer Learning. In *NDSS'21*. The Internet Society.
- [47] Nguyen Anh Quynh. 2014. Capstone: Next-gen disassembly framework. *Black Hat USA* 5, 2 (2014), 3–8.
- [48] radareorg. 2014. Radare2: Libre Reversing Framework for Unix Geeks. <https://github.com/radareorg/radare2>.
- [49] Xiaolei Ren, Michael Ho, Jiang Ming, Yu Lei, and Li Li. 2021. Unleashing the hidden power of compiler optimization on binary code difference: an empirical study. In *PLDI '21*. ACM, 142–157.
- [50] Huanyao Rong, Yue Duan, Hang Zhang, XiaoFeng Wang, Hongbo Chen, Shengchen Duan, and Shen Wang. 2024. Disassembling Obfuscated Executables with LLM. *CoRR* abs/2407.08924 (2024).
- [51] Florent Soudel and Jonathan Salwan. 2015. Triton: A Dynamic Symbolic Execution Framework. In *Symposium on la sécurité des technologies de l'information et des communications (SSTIC)*. Rennes, France, 31–54.
- [52] Benjamin Schwarz, Saumya K. Debray, and Gregory R. Andrews. 2002. Disassembly of Executable Code Revisited. In *WCRE'02*. IEEE, 45–54.
- [53] Eui Chul Richard Shin, Dawn Song, and Reza Moazzezi. 2015. Recognizing Functions in Binaries with Neural Networks. In *24th USENIX Security Symposium*. USENIX Association, 611–626.
- [54] Yan Shoshitaishvili, Ruoyu Wang, Andrew Dutcher, Lukas Dresel, Zion Leona-henahe Basque, Eric Gustafson, Nilo Redini, Paul Grosen, Colin Unger, Christopher Salls, Nick Stephens, Christophe Hauser, Jessie Grosen, Christopher Krügel, and Giovanni Vigna. 2013. angr: A platform-agnostic binary analysis framework. <https://github.com/angr/angr>.
- [55] Yan Shoshitaishvili, Ruoyu Wang, Christopher Salls, Nick Stephens, Mario Polino, Andrew Dutcher, John Grosen, Siji Feng, Christophe Hauser, Christopher Krügel, and Giovanni Vigna. 2016. SOK: (State of) The Art of War: Offensive Techniques in Binary Analysis. In *SP '16*. IEEE, 138–157.
- [56] Asia Slowinska, Traian Stancescu, and Herbert Bos. 2012. Body Armor for Binaries: Preventing Buffer Overflows Without Recompile. In *USENIX Annual Technical Conference*. USENIX Association, 125–137.
- [57] VMProtect Software. 2025. VMProtect. <https://vmpsoft.com/vmprotect/>.
- [58] Rui Sun, Yinggang Guo, Zicheng Wang, and Qingkai Zeng. 2023. AttnCall: Refining Indirect Call Targets in Binaries with Attention. In *ESORICS '23 (LNCS, Vol. 14347)*. Springer, 391–409.
- [59] Oreans Technologies. 2004–2025. Themida: Advanced Windows software protection system. <https://www.oreans.com/themida.php>.
- [60] Ruturaj K. Vaidya, Prasad A. Kulkarni, and Michael R. Jantz. 2021. Explore Capabilities and Effectiveness of Reverse Engineering Tools to Provide Memory Safety for Binary Programs. In *ISPEC '21 (LNCS, Vol. 13107)*. Springer, 11–31.
- [61] Victor van der Veen, Enes Göktas, Moritz Contag, Andre Pawlowski, Xi Chen, Sanjay Rawat, Herbert Bos, Thorsten Holz, Elias Athanasopoulos, and Cristiano Giuffrida. 2016. A Tough Call: Mitigating Advanced Code-Reuse Attacks at the Binary Level. In *SP'16*. IEEE, 934–953.
- [62] Ashish Vaswani, Noam Shazeer, Niki Parmar, Jakob Uszkoreit, Llion Jones, Aidan N. Gomez, Lukasz Kaiser, and Illia Polosukhin. 2017. Attention is All you Need. In *NIPS'17*. 5998–6008.
- [63] Vector 35. 2016. Binary Ninja. <https://binary.ninja>.
- [64] Haijun Wang, Xiaofei Xie, Shang-Wei Lin, Yun Lin, Yuekang Li, Shengchao Qin, Yang Liu, and Ting Liu. 2019. Locating vulnerabilities in binaries via memory layout recovering. In *ESEC/SIGSOFT FSE '19*. ACM, 718–728.
- [65] Shuai Wang, Pei Wang, and Dinghao Wu. 2015. Reassembleable Disassembling. In *24th USENIX Security Symposium*. USENIX Association, 627–642.
- [66] Richard Wartell, Yan Zhou, Kevin W. Hamlen, and Murat Kantarcioglu. 2014. Shingled Graph Disassembly: Finding the Undecidable Path. In *PAKDD '14 (LNCS, Vol. 8443)*. Springer, 273–285.
- [67] Richard Wartell, Yan Zhou, Kevin W. Hamlen, Murat Kantarcioglu, and Bhavani Thuraisingham. 2011. Differentiating Code from Data in x86 Binaries. In *ECML PKDD '11 (LNCS, Vol. 6913)*. Springer, 522–536.
- [68] Yapeng Ye, Zhuo Zhang, Qingkai Shi, Yousra Aafer, and Xiangyu Zhang. 2023. D-ARM: Disassembling ARM Binaries by Lightweight Superset Instruction Interpretation and Graph Modeling. In *SP'23*. IEEE, 2391–2408.
- [69] Sheng Yu, Yu Qu, Xunchao Hu, and Heng Yin. 2022. DeepDi: Learning a Relational Graph Convolutional Network Model on Instructions for Fast and Accurate

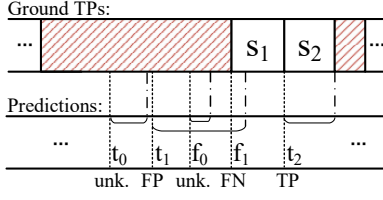


Figure 14: Classification Definition on Incomplete Ground Truths

Tool	SN _{ELF} ⁶⁴	SN _{ELF} ^{x86}	SN _{PE} ⁶⁴	SN _{PE} ^{x86}
DISA	0.999	1.000	0.999	1.000
XDA	0.999	1.000	1.000	1.000
biRNN	0.998	0.999	0.999	0.998
DEEPI	0.998	0.998	0.999	0.998
IDA Pro	0.998	0.993	0.999	0.999
Ghidra	0.960	0.927	0.949	0.968

Figure 15: T2 Accuracy Heatmaps on Different Platforms and ISA Variants

Tool	curl	diffutils	GMP	ImageMagick	libmicrohttpd	libmccrypt	OpenSSL	Putty	SQLite	zlib	Glbc-2.22
DISA	0.999	0.999	0.997	0.999	0.999	0.998	0.998	0.999	0.998	0.998	0.994
XDA	0.999	1.000	0.999	1.000	1.000	0.999	0.999	1.000	0.999	1.000	0.998
biRNN	0.999	0.999	0.997	0.999	0.997	0.992	0.999	0.997	0.999	0.999	0.995
DEEPI	0.999	0.999	0.999	0.998	0.998	0.997	0.999	0.998	0.999	0.999	0.994

Figure 16: T2 Generalizability Heatmap in Predicting Unseen Real-World x64-ELF Binaries

Tool	SO _{ELF} ^{OLL}				SO _{ELF} ^{PE}				SO _{PE} ^{TGR}			
	O0	O1	O2	O3	O0	O1	O2	O3	O0	O1	O2	O3
DISA-SN	0.984	0.979	0.978	0.978	0.984	0.982	0.983	0.983	0.998	0.996	0.998	0.999
XDA-SN	0.997	0.998	0.998	0.998	0.983	0.982	0.983	0.983	1.000	1.000	1.000	1.000
biRNN-SN	0.968	0.961	0.962	0.962	0.974	0.973	0.974	0.974	0.956	0.939	0.998	0.998
DEEPI _{ref}	0.996	0.995	0.995	0.995	0.986	0.986	0.986	0.986	0.998	0.997	1.000	1.000
IDAPro	1.000	1.000	1.000	1.000	0.652	0.485	0.483	0.470	1.000	0.996	1.000	1.000
Ghidra	0.847	0.861	0.901	0.934	0.662	0.595	0.566	0.564	0.766	0.801	0.817	0.844
DISA-SN _{ELF} ⁶⁴	0.999	0.996	0.996	0.996	0.989	0.988	0.988	0.988	0.997	0.996	0.998	0.998
XDA-SN _{ELF} ⁶⁴	0.996	0.998	0.998	0.998	0.985	0.984	0.984	0.984	1.000	0.999	1.000	0.999
biRNN-SN _{ELF} ⁶⁴	0.971	0.987	0.987	0.988	0.975	0.974	0.975	0.975	0.965	0.952	0.998	0.997

Figure 17: T2 Generalizability Heatmap in Predicting Obfuscated Binaries at Different Optimization Levels

- Disassembly. In *31st USENIX Security Symposium*. USENIX Association, 2709–2725.
- [70] Naville Zhang. 2019. Hikari – an improvement over obfuscator-llvm. <https://github.com/HikariObfuscator/Hikari>.
- [71] Zhuo Zhang, Yapeng Ye, Wei You, Guanhong Tao, Wen-Chuan Lee, Yonghui Kwon, Yousra Aafer, and Xiangyu Zhang. 2021. OSPREY: Recovery of Variable and Data Structure via Probabilistic Analysis for Stripped Binary. In *SP'21. IEEE*, 813–832.
- [72] Wenyu Zhu, Zhiyao Feng, Zihan Zhang, Jianjun Chen, Zhijian Ou, Min Yang, and Chao Zhang. 2023. Callee: Recovering call graphs for binaries with transfer and contrastive learning. In *SP'23. IEEE*, 2357–2374.
- [73] zyanific team. 2014. Zydys: The ultimate, open-source X86 & X86-64 decoder/disassembler library. <https://zydis.re>.

A Baseline Implementation and Configuration

We re-implement biRNN using PyTorch following the same structure and setup described in [53]. We especially follow the one-hot encoding of the instruction bytes and the *rmsprop* optimization algorithms, which have yet to be fully adapted in the biRNN re-implementation provided by XDA. We train the biRNN and DISA's

deep models using our datasets. Each biRNN model takes a batch size of 32. XDA models rely on a pre-trained model. In our evaluations, we use the pre-trained model provided by XDA and finetune the XDA models with our datasets. Each epoch for finetuning an XDA model takes several days on an NVIDIA A10 GPU (24GB VRAM) with a 16-core vCPU (60GB RAM). In contrast, the training procedure of a biRNN model is the most efficient, and each epoch takes <2.5 hours and <10 hours for training the DISA-SN_{ELF}^{x64} and DISA-SN models, respectively. We use the default input sequence lengths $L_{\text{biRNN}}=1000$ and $L_{\text{XDA}}=512$. For using the reference model of DEEPI, the *slice length* of the testing dataset has a minor impact on the model's accuracy and generalizability. In our evaluations, we use the default slice length of 1024*1024.

Instruction Ground Truth Collection on Obfuscated Binary. We developed a Pin tool to instrument the SO binaries to record the address and size of each runtime-reached instruction. In this procedure, we input the standard workloads of the SPEC benchmarks and typical test cases for the cryptographic algorithms. Note that we do not use Pin's assembly translation to avoid the impact of its inaccuracy. We calculate the *coverage* of the runtime-reached instructions to the code section and exclude the binaries with *coverage* < 5%. As a result, we obtained SO_{ELF}^{DSY}, SO_{ELF}^{OLL}, and SO_{PE}^{TGR}. The incomplete ground truths of obfuscated binaries require a new definition of classification. As illustrated in Fig. 14, the ground true instructions, e.g., s_1 and s_2 , are spread in segments in the code section, and the instruction segments are separated by *unknown* slots that are unreachable at runtime. The deep models predict on each code byte, e.g., the positive predictions t_0 , t_1 , and t_2 , and the negative predictions f_0 and f_1 . If we disassemble an instruction falling into an unknown slot, e.g., on the byte of t_0 and f_0 , we treat such bytes as unknown instead of positive or negative. If the byte is predicted as an instruction boundary and this instruction has at least one-byte overlap with a true instruction, then this boundary byte has a positive classification. For example, the positive verdict t_1 on a non-instruction byte is a false positive (FP). The negative verdict f_1 on the true instruction s_1 is a false negative (FN). The positive verdict t_2 on the true instruction s_2 is a true positive (TP).

B Evaluation Results Supplementary

Results on Accuracy. The instruction-level deep models take sufficient knowledge of the instruction features on different platforms; thus, the T_2 deep models have $F1 > 99\%$, and the comparative advantages between these models are generally insignificant (Fig. 15).

Results on Generalizability. Fig. 16 illustrates the generalizability of deep models in identifying instructions of unseen real-world binaries in SR_{ELF}^{x64}. Fig. 17 presents the results in identifying instructions of the binaries respectively obfuscated by *ollvm*, *desync-cc*, and *tigris*. DISA's x64ELF-centric model outperforms other approaches to identify the instructions of the *desync-cc*-obfuscated binaries. Due to the dynamic approach to obtaining the incomplete ground truths of SO, the classification errors (FPs and FNs) can only arise on the superset instructions that overlap with the runtime-reached true instructions. We further investigate how the code coverage of the ground true instructions impacts the detection results, as the higher code coverage implies fewer model predictions falling in the

Table 5: Generalizability on Task T_2 to Predict Obfuscated Binaries with Different Code Coverage in Ground Truth Collection

Model	SO ^{OLL} _{ELF}								SO ^{DSY} _{ELF}								SO ^{TGR} _{PE}							
	Code Coverage(#Binaries)								Code Coverage(#Binaries)								Code Coverage(#Binaries)							
	5%-30%(25)		30%-50%(31)		50%-75%(39)		75%-100%(5)		5%-30%(31)		30%-50%(26)		50%-75%(33)		75%-100%(9)		5%-30%(56)		30%-50%(4)					
	P	R	P	R	P	R	P	R	P	R	P	R	P	R	P	R	P	R	P	R				
Disa-SN ^{x64} _{ELF}	.998	.998	.997	.998	.996	.997	.996	.997	.981	.996	.981	.996	.980	.995	.982	.997	.997	.998	.999	.999				
XDA-SN ^{x64} _{ELF}	.996	.995	.998	.997	.998	.997	.998	.997	.976	.992	.977	.992	.976	.991	.978	.993	1.00	.999	1.00	1.00				
biRNN-SN ^{x64} _{ELF}	.979	.969	.981	.979	.985	.984	.986	.986	.972	.978	.972	.977	.970	.975	.970	.979	.966	.981	.998	.998				

Table 6: Number of Trainable Parameters of Deep Models

	biRNN	DEEPI	DISA	XDA
#Parameters	8.8k	49.9k	12.9M	86.8M

Table 7: Configurations of Different BPA Variants

Configuration Notation	T_1			T_2			T_3	
	IDA	DISA	BPA	IDA	DISA	BPA	DISA	BPA
BPA			●			●		●
BPA _{DISA}			●			●	●	
BPA _{T1} _{DISA}		●				●	●	
BPA _{T2} _{DISA}			●		●		●	
BPA _{T12} _{DISA}		●			●		●	
BPA _{IDA1} _{DISA}	●					●	●	
BPA _{IDA2} _{DISA}			●	●			●	
BPA _{IDA12} _{DISA}	●			●			●	
BPA _{T1, IDA2} _{DISA}		●		●			●	
BPA _{T2, IDA1} _{DISA}	●				●		●	

unknown slots, and the detection results are closer to the results on complete ground truths. We use the x64ELF-centric deep models. Table 5 presents the results at different code coverages. Generally, we did not observe remarkable decreases in precision and recall along with increased code coverage of ground true instructions. The results justify our strategy of obtaining the incomplete ground truths at runtime.

Results on Efficiency. Besides comparing the time cost in Section 5.6, the prediction cost of different learning-based approaches

can be estimated by comparing the number of trainable parameters of deep models, as presented in Table 6.

Results on extended ablation study. In our extended ablation study, we investigated a range of combinations of instruction and function boundaries derived from IDA, the original BPA, and DISA’s three tasks. As illustrated in Table 7, we developed several BPA variants by incorporating different instruction and function boundaries alongside a memory block boundary detection module either from DISA’s T_3 or from original BPA. The performance outcomes for these variants, measured in terms of AICT and Recall, are presented in Table 8. For clarity, we excluded bzip2, sphinx3, and a few optimized versions of milc, sjeng, hmmer, and h264ref, as all these instances yielded identical AICT results with a 100% recall rate across all variants. Furthermore, we had to omit GCC from our study due to time constraints, as detailed in Section 5.5.4. Table 8 demonstrates that our BPA variants, particularly BPA_{DISA}^{T12}, achieved results that are either comparable to or superior to other versions. The IDA-supported variants, including BPA_{DISA}^{IDA12}, BPA_{DISA}^{IDA2}, BPA_{DISA}^{IDA1}, and BPA_{DISA}^{T2, IDA1}, have demonstrated comparable performance, especially for lower optimized binaries, i.e., hmmer-00, h264ref-00, gobmk-00, and perlbench-00. The BPA_{DISA}^{T1, IDA2}, which takes IDA instruction boundaries and DISA function boundaries, has also matched the performance of BPA_{DISA}^{T12} for sjeng-01, h264ref-00, 01, hmmer-00, gobmk, as well as perlbench-01 and 02. This suggests that DISA T_1 can enhance the performance of IDA-supported BPA variants as well. Nonetheless, BPA_{DISA}^{T12} continues to outperform all others by delivering the best overall improvements.

Table 8: AICT and Recall across Different BPA Variants

[illegible]